Computational and Applied Mathematics (2022) 41: 312
https://doi.org/10.1007/s40314-022-01995-z

Prediction of thermal and energy transport of MHD Sutterby hybrid nanofluid flow with activation energy using Group Method of Data Handling (GMDH)

S. Gopi Krishna[1] · M. Shanmugapriya[1] · Ammar Alsinai[2] · Abdu Alameri[3]

Received: 7 May 2022 / Revised: 10 July 2022 / Accepted: 6 August 2022 /
Published online: 14 September 2022
© The Author(s) under exclusive licence to Sociedade Brasileira de Matemática Aplicada e Computacional 2022

Abstract
The present research work pursues GMDH for predicting thermal and energy transport of 2-D radiative magnetohydrodynamic (MHD) flow of hybrid Sutterby nanofluid across a moving wedge with activation energy. An exclusive class of nanoparticles SWCNT–Fe_3O_4 and MWCNT–Fe_3O_4 are dispersed into the ethylene glycol as regular fluid. The hybrid nanofluid mathematical model has been written as a system of partial differential equations (PDEs), which are then converted into ordinary differential equations (ODEs) through similarity replacements. Numerical solutions are attained Runge–Kutta–Fehlberg's fourth fifth-order (RKF-45) scheme by adopting the shooting technique. The ranges of diverse sundry parameters used in our study are Hartree parameter $0.1 \le m \le 0.5$, magnetic parameter $0.3 \le M \le 1$, Deborah number $0.1 \le \mathrm{De} \le 1$, moving wedge parameter $0.3 \le \gamma \le 0.9$, Reynolds number $0 \le \mathrm{Re} \le 2.5$, solid volume fraction of Fe_3O_4 and CNT$s 0.005 \le \varphi_1 \le 0.1, 0.005 \le \varphi_2 \le 0.06$, Browanian motion $0.1 \le \mathrm{Nb} \le 0.4$, thermophoresis parameter $0.1 \le \mathrm{Nt} \le 0.25$, Eckeret number $0.05 \le \mathrm{Ec} \le 1$, radiation parameter $1 \le R_\mathrm{d} \le 2.5$, Lewis number $0.5 \le \mathrm{Le} \le 1.5$, chemical reaction rate $0.1 \le \sigma \le 0.7$, heat source parameter, $0 \le \delta \le 1.5$ and activation energy $1 \le E \le 4$ which shows up during the speed, thermal, and focus for $Fe_3O_4/C_2H_6O_2$ nanofluid and CNTs$-Fe_3O_4/C_2H_6O_2$ hybrid nanofluid. Additionally, the friction coefficient ($\breve{C}_{fx}$), rate of heat transport ($\breve{H}_{tx}$), and rate of nanoparticle transport ($\breve{N}t_x$ are calculated using GMDH. The numerical results for the current analysis are illustrated via tables, graphs, and contour plots. The efficiency of the proposed GMDH models is assessed using statistical measures such as MSE, MAE, RMSE, R, Error mean and Error StD. The predicted values are very close to the numerical results,

Communicated by Zdenko Takac.

✉ Abdu Alameri
a.alameri2222@gmail.com

1 Department of Mathematics, Sri Sivasubramaniya Nadar College of Engineering, Kalavakkam 603110, India

2 Department of Mathematics, University of Mysore, Mysore, Karnataka, India

3 Department of Biomedical Engineering, Faculty of Engineering, University of Science and Technology, Taiz, Yemen

and the coefficient of determination R^2 of $\breve{C}_{fx}$, $\breve{N}_{tx}$, and $\breve{H}t_x$ are 1, 0.97836 and 0.9960, respectively, which shows the best settlement.

Keywords Hybrid Sutterby nanofluid · Activation energy · Fe_3O_4/C_2H_6O2 · CNTs–$Fe_3O_4/C_2H_6O_2$ · GMDH

Mathematics Subject Classification 34A38 · 35B38 · 81T17

List of symbols

$\overrightarrow{q}$	Velocity vector, (m/s)
P	Pressure, (N/m^2)
S	Sutterby nanofluid
$\overrightarrow{J}$	Current density
$\overrightarrow{B}$	External magnetic field
D_{B}, D_{T}	Brownian and thermophoresis diffusion coefficient, (m^2/s)
$\breve{q}_{\mathrm{r}}$	Radiative heat flux, (W/m^2)
$\breve{T}_{\mathrm{w}}$, $\breve{T}_\infty$	Temperature near and far away from the wedge surface, (K)
$\breve{T}$	Temperature of the hybrid nanofluid, (K)
$\breve{C}$	Concentration of the hybrid nanofluid, (moles/kg)
${k_{\mathrm{r}}}^2$	Rate of chemical reaction, (1/s)
$\breve{C}_w$, $\breve{C}_\infty$	Concentration near and far away from the wedge surface, (moles/m^3)
$\breve{N}_0$	Fitted rate constant
E_a	Modified Arrhenius function, (J)
n	Materials constant
$\acute{A}_1$	First tensor of Rivlin–Erickson
$\acute{\Lambda}$	Second invariant strain tensor
$\breve{u}$, $\breve{v}$	Velocity components of $\breve{x}$ and $\breve{y}$ directions, (m/s)
$\breve{x}$	Distance along the surface, (m)
$\breve{y}$	Distance normal to the surface, (m)
k_0	Physical constant
f	Dimensionless velocity
$\breve{C}_{fx}$	Friction coefficient, (pascal)
$\breve{H}_{tx}$	Rate of heat transport
$\breve{N}\, t_x$	Rate of nanoparticle transport
Re	Reynolds number
M	Magnetic parameter
m	Hartree pressure gradient
De	Deborah number
$\breve{u}_{\mathrm{w}}$, $\breve{U}_\infty$	Velocities near and far away from the surface, (m/s)
Pr	Prandtl number
De	Deborah number
R_{d}	Radiation parameter
Nb	Brownian motion parameter

Nt	Thermophoresis parameter
Ec	Eckert number
Le	Lewis number
E	Activation energy, (J)
B_0	Magnetic induction parameter, (T)

Greek symbols

ξ	Similarity variable
τ	Cauchy stress tensor
ψ	Stream function
σ_{bf}	Electrical conductivity of the base fluid, (S/m)
σ^*	Stefan–Boltzmann constant, (W/m^2 K^4)
k^*	Mean absorption coefficient, (1/m)
Φ	Viscous dissipation
$\acute{\mu}_0$	Viscosity at the low sheer rates
$\dot{\omega}$	Sheer stress
$\widehat{\beta}_1$	Materials constant
θ	Dimensionless temperature
ϕ	Dimensionless concentration
γ	Wedge moving parameter
φ_1, φ_2	Solid volume fraction of Fe_3O_4 and CNTs
σ	Chemical reaction rate
δ	Heat source parameter
$\breve{\Omega}^*$	Total wedge angle
λ	Wedge angle parameter
ϑ_{bf}	Kinematic viscosity of the base fluid, (m^2/s)
μ_{bf}	Dynamic viscosity of the base fluid, (kg/m s)
ρ_{bf}	Density of the base fluid, (kg/m^3)
k_{bf}	Thermal conductivity of the base fluid, (W/m K)
$(\rho c_{\mathrm{p}})_{\mathrm{bf}}$	Effective heat capacity of the base fluid, (kg/m^{3}K)
ρ_{nf}	Density of the nanofluid, (kg/m^3)
$(\rho c_{\mathrm{p}})_{\mathrm{nf}}$	Heat capacity of the nanofluid, (kg/m^3 K)
k_{nf}	Thermal conductivity of the nanofluid, (W/m K)
ϑ_{nf}	Kinematic viscosity of the nanofluid, (m^2/s)
μ_{nf}	Dynamic viscosity of the nanofluid, (kg/m s)
ρ_{hnf}	Effective dynamic density of the hybrid nanofluid, (kg/m^3)
$(\rho c_{\mathrm{p}})_{\mathrm{hnf}}$	Volumetric heat capacity of the hybrid nanofluid, (kg/m^3 K)
μ_{hnf}	Dynamic viscosity of the hybrid nanofluid, (kg/m s)
k_{hnf}	Thermal conductivity of the ternary hybrid nanofluid, (W/m K)
ϑ_{hnf}	Kinematic viscosity of the hybrid nanofluid, (m^2/s)

Subscripts

bf	Base fluid
nf	Nanofluid

hnf	Hybrid nanofluid
w	Quantities at wall
∞	Quantities at free stream

1 Introduction

The diverse rheological nature and assorted physiological and industrial applications of non-Newtonian fluid motivated researchers to urge diverse rheological models. Each model confiscation some precise rheological features. Among those, the Sutterby rheological model (Sutterby 1966) is non-Newtonian rheological models that exhibit high polymer aqueous solutions. This rheological model mirrors the viscosity measurements of a broad range of polymer melts and solutions. The feature of the non-Newtonian rheological model is represented by this viscous model, which is an intriguing feature. Hayat et al. (2017) have described the properties of Sutterby fluid using Darcy's relation. Khan et al. (2019) have discussed heat transfer of Sutterby fluid flow by rotating disk with chemical phenomena through Cattaneo–Christov model. Fayyadh et al. (2020) have studied Sutterby nanoliquid radiative MHD flow through the permeable moving sheet with established surface convective heat flux utilizing bvp4c. Besthapu et al. (2019) examined the repercussion of warmth radiation and velocity slip from the MHD stream of non-Newtonian fluid configured by a nonlinearly stretching sheet. Sabir et al. (2021) studied the effects of thermal radiation and inclined magnetic field on the Sutterby fluid by utilizing the Cattaneo–Christov heat flux system. Sajid et al. (2022) have revealed the impact of gold blood nanoparticles along with Maxwell velocity and smoluchowski temperature slip boundary conditions on the Sutterby fluid model. A sweeping review of Sutterby nanofluid flow and heat transfer applications have been suggested in Mir et al. (2020), Khan et al. (2021a) and Ramesh et al. (2021).

Nanofluid is a revolutionary heat transfer fluid that is created by dissipating nonmetallic or metallic nanoadditives with a normal size of less than 100 nm nanometers in a regular fluid. Coolants including motor oil, propane, water, and other coolants such as metals, nonmetals, and carbon nanotubes have too little warm conductivity. The thermic transmit rate addresses the coolant's thermodynamic highlights. This can be upgraded by incorporating nanoscale particles into refrigerants. These nanofluids are applied in technical usances such as transportation, microelectronics, solar thermal, computer processors, and mobile phones. Choi and Eastman (1995) were the first to claim that nanoliquids had a greater heat transfer rate than pure fluids. Nanoparticles silver (Ag) with base fluids like water and kerosene past an exponentially shrinking permeable sheet under the impact of momentum slip and warmth slip was examined by Ghosh and Mukhopadhyay (2020). Hayat et al. (2019a) have investigated the 3-D MHD stream of viscoelastic nanomaterials around an impermeable stretching surface. Many researchers have addressed the various types of nanoparticles with sundry physical aspects such as heat radiation, heat generation, and viscous dissipation (Shanmugapriya 2018; Ferdows et al. 2021; Jusoh et al. 2019; Elayarani et al. 2019; Amer Qureshi 2021).

Hybrid nanofluids are a unique and advanced variety of nanofluids. It is a balanced blend of two different solid nanoadditives dispersed in a regular fluid. The primary idea behind hybrid nanoliquids is to produce remarkable heat transfer efficiency and extremely useful thermal conductivity in analogy to regular heat transfer fluids and nanofluids. Consequently, hybrid nanoliquids have been used in a vast of heat transmission applications, including heat exchangers, mini-channel heat sink, micro-channel, air conditioning systems, and heat pipes, (Shanmugapriya et al. 2021; Waini et al. 2022; Zainal et al. 2021). Turcu et al. (2006) first created a hybrid nanofluid with the inclusion of Fe_3O_4 nanoparticles on MWCNTs utilizing polypyrrole polymerization. Furthermore, Jana et al. (2007 discovered the upgrade of liquid thermic conductivity by the incorporation of individual and hybrid nanoadditives. Suresh et al. (2011) investigated the manufacture of hybrid Al_2O_3--Cu/H_2O nanoliquids using a second-step technique. Nawaz (2020) utilizing the finite element method, has scrutinized the vigor of hybrid nano materials (MoS_2 and SiO_2) for varying the thermal ability of Sutterby fluid taking ethylene glycol as a conventional liquid. The effect of the magnetic parameter, suction, and non-linear thermal radiation on Cu--Al_2O_3/H_2O--$C_2H_6O_2$ hybrid nanofluids along a stretched surface were addressed by Khan et al. (2019). Ayub et al. (2021) have investigated the heat and mass transfer of magnetized chemically radiative hybrid nanofluid (Ag--Al_2O_3/H_2O) along rotating sheet. Besides, Wahid et al. (2021) and Waini et al. (2022) studied the heat transmission analysis of Cu--Al_2O_3/water-based hybrid nanoliquid in different geometries.

Carbon nanotubes (CNTs) are molecules settled in a cylindrical way which consists of sheets that are surrounded by graphene. Owing to the graphene sheet, CNTs are subdivided into MWCNTs (cylindrical carbon materials surrounded by more than one graphene layer) and SWCNTs (cylindrical carbon material fenced by one graphene layer). CNTs are vastly adept nanotubes as they have 6 times greater mechanical, physicochemical highest thermal conductivity, lightweight density than other nanostructure materials. CNTs performance an essential role in the area of engineering, chemical manufacturing, optics, microelectronic cooling and material science. The concept of CNTs was originally invented in 1991 by Lijima (1991). Ameen et al. (2019) have explored the consequence of hall current and iron-slip on 3-D stream on kerosine-based CNTs past a permeable stretching surface. Hayat et al. (2019b) have discovered the analytical solutions of Darcy–Forchheimer flow of water-based CNTs induced by a rotating disc convectively heated using OHAM. The ethylene glycol-based nanofluid flow containing CNTs of both categories under the effect of MHD, thermal slip, and modified heat flux amid rotating stretchable disc was examined by Tulu and Ibrahim (2020). Sajid et al. (2021) examined the effects of Maxwell velocity slip and Smoluchowski temperature slip on CNTs of Reiner–Philippoff model using modified Fourier theory. Recent studies involving carbon nanotubes and magnetite amalgamated fluid flow can be found in Sajid et al. (2021), Tassaddiq et al. (2020), Saba et al. (2019), Bilal et al. (2021), Tulu and Ibrahim (2021) and Saeed et al. (2021) and many others.

In 1889, Svante Arrhenius proposed the phrase "activation energy". It is the least obligatory energy required by a chemical process containing potential reagents to produce a chemical reaction. This phenomenon has a broad range of applications in the fields of chemical engineering, oil emulsion, food processing, geothermal engineering, oil reservoirs etc. Initially, the free convection flow of binary blend in a permeable space with activation energy was suggested by Bestman (1990). Sajid et al. (2020) have scrutinized the dynamic behavior of Maxwell–Sutterby nano liquid under the influence of activation energy and thermal source-sink which can transmit heat. Umar et al. (2019) have discussed the effect of velocity slip and activation energy of three-dimensional Eyring–Powell fluid flow over a stretching surface. Further, the consequence of activation energy in the binary chemically reactive flow of hybrid nanoliquids with numerous features has been reviewed by some authors (Prashar and Ojjela 2022; Ramesh and Madhukesh 2021; Swain et al. 2022).

Group Method of Data Handling (GMDH) algorithm is a self-organizing approach for solving a variety of complex or nonlinear problems. It is used to find the data modeling for complex problems and provides optimal solutions. In recent days, GMDH has grown very fast because of this model highly efficient model to provide solutions for complex problems. It is applied in many areas for discovering knowledge, data mining, optimization, and complex pattern recognition. It used many applications such as image processing, resource management, software, chemical, and health. Initially, the GMDH model was developed by Ivakhnenko (1971). Li et al. (2020) have investigated the development of artificial intelligence based on various techniques to predict the iron ore price. Their outcomes showed that the GMDH method is highly efficient than the other techniques. Atashrouz and Rahmani (2020) have examined the accuracy of the GMDH technique to predict the hydrogen storage capacity of metal–organic frameworks. Mathew Nkurlu et al. (2020) have estimated the permeability of well log data using the GMDH neural network. Fathi et al. (2020) have employed the GMDH network for experimental data of the heat transfer between curve-linear contact geometries using the inverse technique. The application of the GMDH network can be helpful for finding the solution to nonlinear systems of the hybrid nanofluid flow of the Sutterby model in the presence of thermal radiation and activation energy.

To the best of the author's knowledge from the above-mentioned literature survey, thermal and energy transport of MHD Sutterby hybrid nanofluid flow with activation energy using the GMDH network is not reported yet. These hybrid nanofluid flows of the Sutterby model have been applied in the energy sectors such as electrolytes, steam generators, concrete heating, laminating, catalysis and oil emulsion. As a result, the present work focuses on this topic. A novel architecture of data handling method, GMDH is incorporated for predicting friction coefficient ($\breve{C}_{fx}$), rate of heat transport $\left(\breve{H}_{tx}\right)$, and rate of nanoparticle transport ($\breve{N}t_x$) of MHD Sutterby hybrid nanofluid. With adequate thermal radiation and activation energy with binary chemical reaction, the dynamic model is transformed into a system of ODEs. To obtain the numerical results, the RKF-45 assimilation scheme together with the shooting method is used. The efficiency and performance of GMDH network model is verified by comparing the results with the numerical solution of the MHD Sutterby hybrid nanofluid through analyzes of error, graphical outcomes of statistical validation errors and R^2. It converges expeditiously with the numerical results, and the efficiency of the results is quite sound.

2 Mathematical formulation

2.1 Physical configuration

Thermal and energy transportation for the steady 2-D incompressible radiative magnetohydrodynamic flow of hybrid nanoparticles (CNTs$-Fe_3O_4/C_2H_6O_2$) in Sutterby nanofluid across a moving wedge with activation energy has been considered. The expressions $\breve{u}_e\left(\breve{x}\right) = \breve{U}_\infty \breve{x}^m$ and $\breve{u}_w\left(\breve{x}\right) = \breve{U}_w \breve{x}^m$ depicts the free stream and stretching velocity. Here $\lambda = \frac{2m}{m+1}$, where m and Î» are the power law index and the angle parameter of wedge respectively, while the total angle of the wedge is defined by $\lambda\pi = \breve{\Omega}^*$. The temperature and nanoparticle concentration of the wedge surface are $\breve{T}_w$ and $\breve{C}_w$ while the ambient temperature and nanoparticle concentration of the hybrid Sutterby nanofluid are $\breve{T}_\infty\left(< \breve{T}_w\right)and\breve{C}_\infty\left(< \breve{C}_w\right)$, respectively. The magnetic field intensify $\breve{b}\left(\breve{x}\right) = B_0 \breve{x}^{\frac{m-1}{2}}$ is carried out perpendicularly to the surface of a wedge as shown in Fig. 1. The vector form of the governing equations of the present physical flow problem can be expressed as follows (Ramesh et al. 2021; Haider et al. 2021):

$$\nabla \cdot \overrightarrow{q} = 0, \tag{1}$$

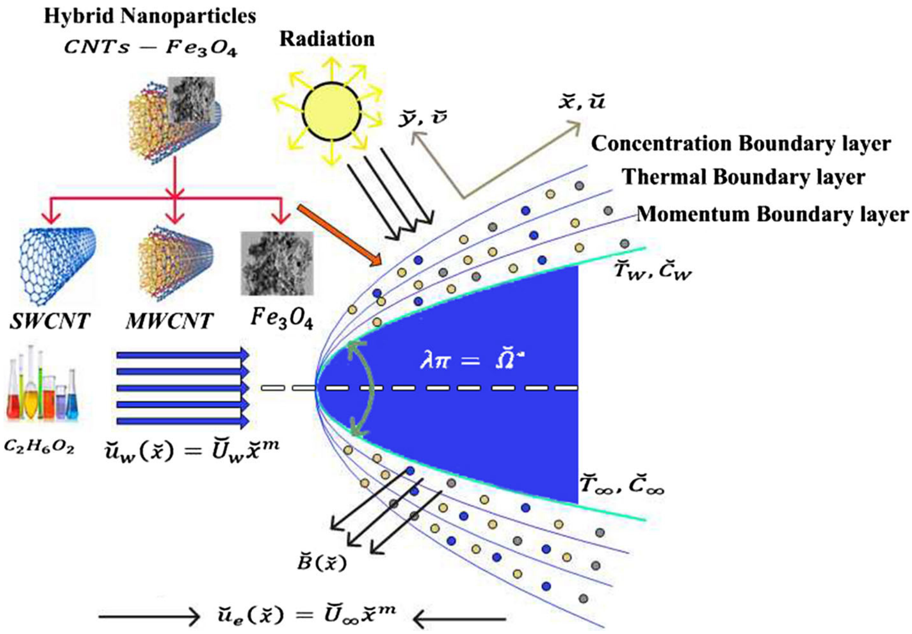

Fig. 1 Systematic diagram for the flow field

$$\rho_{\mathrm{hnf}}\left[\left(\vec{q}\cdot\nabla\right)\vec{q}\,\right] = -\nabla \mathrm{P} + \nabla\cdot S + \vec{J}\times\vec{B}, \tag{2}$$

$$\left(\rho c_{\mathrm{p}}\right)_{\mathrm{hnf}}\left[\left(\vec{q}\cdot\nabla\right)\breve{T}\right] = \nabla\cdot\left(k_{\mathrm{hnf}}\nabla\breve{T}\right) - \nabla\cdot\breve{q}_{\mathrm{r}} + \tau\left[D_{\mathrm{B}}\nabla\breve{C}\cdot\nabla\breve{T} + \frac{D_T}{\breve{T}_\infty}\left(\nabla\breve{T}\cdot\nabla\breve{T}\right)\right] + \mu_{\mathrm{hnf}}\Phi, \tag{3}$$

$$\left(\vec{q}\cdot\nabla\right)\breve{b} \stackrel{C}{=} D_{\mathrm{B}}\nabla^2\breve{C} + \frac{D_T}{\breve{T}_\infty}\nabla^2 - k_{\mathrm{r}}{}^2\left(\breve{C}-\breve{C}_\infty\right)\left(\frac{\breve{T}}{\breve{T}_\infty}\right)^{\breve{N}_0}\exp^{\left(\frac{-E_{\mathrm{a}}}{k_{\mathrm{bf}}\breve{T}_\infty}\right)}. \tag{4}$$

here, $\vec{q} = \left[\breve{u}\left(\breve{x},\breve{y}\right), \breve{v}\left(\breve{x},\breve{y}\right)\right], \breve{T} = \breve{T}\left(\breve{x},\breve{y}\right), \breve{C} = \breve{C}\left(\breve{x},\breve{y}\right)$ and $\vec{J}\times\vec{B} = -\sigma_{bf}\breve{b}\,\vec{q}$ denote the velocity, temperature, concentration vectors and the Lorentz force, respectively. Moreover, $\breve{q}_r$ is the radiative heat flux and $\Phi = 1 - \frac{\widehat{\beta}_1^2}{6}\left[4\left(\frac{\partial\breve{u}}{\partial\breve{x}}\right)^2 + \left(\frac{\partial\breve{u}}{\partial\breve{y}} + \frac{\partial\breve{v}}{\partial\breve{x}}\right)^2\right]^n$ is the viscous dissipation function.

2.2 Flow description

The rheological model of stress tensor and incompressible flow of a Sutterby nanofluid can be followed as in Haider et al. (2021)

$$S = \acute{\mu}_0\left(\frac{\sin h^{-1}\left(\widehat{\beta}_1\dot{\omega}\right)}{\widehat{\beta}_1\dot{\omega}}\right)^n \acute{A}_1, \tag{5}$$

with

$$\acute{A}_1 = \left(\nabla\overrightarrow{q}\right) + \left(\nabla\overrightarrow{q}\right)^{\mathrm{T}}, \tag{6}$$

$$\dot{\omega} = \sqrt{\sum_i\sum_j \dot{\omega}_{1i}\dot{\omega}_{j1}} = \sqrt{\frac{\acute{\Lambda}}{2}}, \tag{7}$$

$$\acute{\Lambda} = \mathrm{trace}\left(\acute{A}_1\right)^2, \tag{8}$$

In the above expressions $\widehat{\beta}_1$ and n are the materials constant, whereas $\acute{\mu}_0$, $\dot{\omega}$, $\acute{A}_1$ and $\acute{\Lambda}$ denote the viscosity at the low sheer rates, the sheer stress, the first tensor of Rivlin–Erickson and the second invariant strain tensor, respectively. Using the expansion of $\sin h^{-1}$ by Taylor's series approximation, and as $\widehat{\beta}_1\dot{\omega} << 1$, we have the viscosity of Sutterby nanofluid is

$$\mu = \acute{\mu}_0\left(\frac{sinh^{-1}\left(\widehat{\beta}_1\dot{\omega}\right)}{\widehat{\beta}_1\dot{\omega}}\right)^n \cong \acute{\mu}_0\left(1 - \frac{\left(\widehat{\beta}_1\dot{\omega}\right)^2}{6}\right)^n. \tag{9}$$

In view of the foregoing assumptions, the boundary layer equations of hybrid Sutterby nanofluid are expressed as (Shanmugapriya et al. 2021; Khan et al. 2020; Gopi Krishna and Shanmugapriya 2021),

$$\frac{\partial\breve{u}}{\partial\breve{x}} + \frac{\partial\breve{v}}{\partial\breve{y}} = 0, \tag{10}$$

$$\begin{aligned}\left(\breve{u}\frac{\partial\breve{u}}{\partial\breve{x}} + \breve{v}\frac{\partial\breve{u}}{\partial\breve{y}}\right) = {} & \breve{u}_e\frac{d\,\breve{u}_e}{d\breve{x}} + \vartheta_{\mathrm{hnf}}\frac{\partial^2\breve{u}}{\partial\breve{y}^2}\left(1 - \frac{\hat{\beta}_1^2}{6}\left(\frac{\partial\breve{u}}{\partial\breve{y}}\right)^2\right)^n \\ & - \vartheta_{\mathrm{hnf}}\frac{\partial^2\breve{u}}{\partial\breve{y}^2}\frac{n\hat{\beta}_1^2}{3}\left(\frac{\partial\breve{u}}{\partial\breve{y}}\right)^2\left(1 - \frac{\hat{\beta}_1^2}{6}\left(\frac{\partial\breve{u}}{\partial\breve{y}}\right)^2\right)^{n-1} + \frac{\sigma_{\mathrm{bf}}\tilde{B}^2(x)}{\rho_{\mathrm{hnf}}}\left(\breve{u}_e - \breve{u}\right)\end{aligned} \tag{11}$$

$$\begin{aligned}\left(\breve{u}\frac{\partial\breve{T}}{\partial\breve{x}} + \breve{v}\frac{\partial\breve{T}}{\partial\breve{y}}\right) = {} & \frac{k_{\mathrm{hnf}}}{\left(\rho c_{\mathrm{p}}\right)_{\mathrm{hnf}}}\frac{\partial^2\breve{T}}{\partial\breve{y}^2} + \frac{\mu_{\mathrm{hnf}}}{\left(\rho c_{\mathrm{p}}\right)_{\mathrm{hnf}}}\left(1 - \frac{\hat{\beta}_1^2}{6}\left(\frac{\partial\breve{u}}{\partial\breve{y}}\right)^2\right)^n\left(\frac{\partial\breve{u}}{\partial\breve{y}}\right)^2 \\ & + \tau\left(D_{\mathrm{B}}\frac{\partial\breve{T}}{\partial\breve{y}}\left(\frac{\partial\breve{C}}{\partial\breve{y}}\right) + \frac{D_T}{\breve{T}_\infty}\left(\frac{\partial\breve{T}}{\partial\breve{y}}\right)^2\right) - \frac{1}{\left(\rho c_{\mathrm{p}}\right)_{\mathrm{hnf}}} \times \frac{\partial\breve{q}_r}{\partial\breve{y}},\end{aligned} \tag{12}$$

$$\left(\breve{u}\frac{\partial\breve{C}}{\partial\breve{x}} + \breve{v}\frac{\partial\breve{C}}{\partial\breve{y}}\right) = D_{\mathrm{B}}\frac{\partial^2\breve{C}}{\partial\breve{y}^2} + \frac{D_T}{\breve{T}_\infty}\frac{\partial^2\breve{T}}{\partial\breve{y}^2} - k_r^2\left(\breve{C} - \breve{C}_\infty\right)\left(\frac{\breve{T}}{\breve{T}_\infty}\right)^{\tilde{n}_0}\exp^{\left(\frac{-E_a}{k_{bf}\breve{T}_\infty}\right)}. \tag{13}$$

Related boundary constraints are

$$\breve{u}(\breve{x},0) = \breve{u}_{\mathrm{w}}\left(\breve{x}\right),\ \breve{v}(\breve{x},0) = 0,\ \breve{T} = \breve{T}_{\mathrm{W}},\ \breve{C} = \breve{C}_{\mathrm{W}},\ \mathrm{at}\,\breve{y} = 0, \tag{14}$$

$$\breve{u}\left(\breve{x},\infty\right) \to \breve{u}_{\mathrm{e}},\ \breve{T} \to \breve{T}_\infty,\ \breve{C} \to \breve{C}_\infty,\ \mathrm{at}\,\breve{y} = \infty. \tag{15}$$

where $\left(\breve{u}, \breve{v}\right)$ represents the velocity ingredients of nanofluid in $\breve{x}$ and $\breve{y}$, respectively. $\vartheta_{\text{hnf}}, \rho_{\text{hnf}}, k_{\text{hnf}}, \mu_{\text{hnf}}$ and $\left(\rho c_{\text{p}}\right)_{\text{hnf}}$ are the kinematic viscosity, density, thermal conductivity, dynamic viscosity and heat capacity of the hybrid nanofluid, σ_{bf} is the electrical conductivity of the base fluid, τ is the ratio of heat capacity of the nanoparticle, D_{B} and D_{T} are the Brownian and thermophoresis diffusion coefficient, respectively. Furthermore, in Eq. (13), E_{a} is the modified Arrhenius function, k_{r} is the rate of chemical reaction in which $k_{\text{r}}{}^{2} = k_0 \breve{x}^{m-1}$, k_0 is the physical constant.

The radiative heat flux q_{r} is described by the Rosseland approximation as follows:

$$q_{\text{r}} = \frac{-4\sigma^*}{3k^*}\frac{\partial \breve{T}^4}{\partial \breve{y}}, \tag{16}$$

where σ^* and k^* represent the Stefan–Boltzmann constant and mean absorption coefficient, respectively. It is noted that the Rosseland approximation limits the current analysis to fluids that are optimally thick. Because $\breve{T}^4$ can be expressed as a linear function of temperature, we assume that the temperature difference on the flow is very small.

Consequently, neglecting higher-order terms while expanding $\breve{T}^4$ in a Taylor series about $\breve{T}_\infty$, we get

$$\breve{T}^4 \equiv 4\breve{T}_\infty^3 \breve{T} - 3\breve{T}_\infty^4, \tag{17}$$

Utilizing (16) in (17), we obtain

$$\frac{\partial \breve{q}_r}{\partial \breve{y}} = \frac{-16\sigma^* T_\infty{}^3}{3k^*}\frac{\partial^2 \breve{T}}{\partial \breve{y}^2}, \tag{18}$$

Using Eq. (18), the Eq. (12) was reduced to

$$\left(\breve{u}\frac{\partial \breve{T}}{\partial \breve{x}} + \breve{v}\frac{\partial \breve{T}}{\partial \breve{y}}\right) = \frac{k_{\text{hnf}}}{\left(\rho c_{\text{p}}\right)_{\text{hnf}}}\frac{\partial^2 \breve{T}}{\partial \breve{y}^2} + \frac{\mu_{\text{hnf}}}{\left(\rho c_{\text{p}}\right)_{\text{hnf}}}\left(1 - \frac{\hat{\beta}_1^2}{6}\left(\frac{\partial \breve{u}}{\partial \breve{y}}\right)^2\right)^n \left(\frac{\partial \breve{u}}{\partial \breve{y}}\right)^2$$
$$+ \tau\left(D_{\text{B}}\frac{\partial \breve{T}}{\partial \breve{y}}\left(\frac{\partial \breve{C}}{\partial \breve{y}}\right) + \frac{D_{\text{T}}}{\breve{T}_\infty}\left(\frac{\partial \breve{T}}{\partial \breve{y}}\right)^2\right) + \frac{16\sigma^* T_\infty^3}{3k^*\left(\rho c_{\text{p}}\right)_{\text{hnf}}} \times \frac{\partial^2 \breve{T}}{\partial \breve{y}^2}. \tag{19}$$

2.3 Thermo-physical attributes of $CNTs$ hybrid nanofluid

The hybrid nanofluid includes the nanoparticles CNTs and Fe_3O_4 suspended in regular fluid ethylene glycol ($C_2H_6O_2$). Table 1 exhibits the mathematical relation for the thermo physical attributes of nanofluid as well as hybrid nanofluid. Here, φ_1 and φ_2 are the solid volume fractions of Fe_3O_4 and CNTs. The variables $\rho_{\text{s1}}, \rho_{\text{s2}}, \left(\rho c_{\text{p}}\right)_{\text{s1}}, \left(\rho c_{\text{p}}\right)_{\text{s2}}, k_{\text{s1}}$ and k_{s2} represent the densities, heat capacity and thermal conductivity of Fe_3O_4 and CNTs nanocomposites, respectively. The thermophysical characteristic of base solvent and nano materials are listed in Table 2 (Gul et al. 2020; Ghadikolaei et al. 2018).

Table 1 Thermo-physical characteristics of the nanofluid and hybrid nanofluid (Waini et al. 2020b; Ali et al. 2021)

Property	Nanofluid	Hybrid nanofluid
Dynamic viscosity (μ)	$\mu_{\mathrm{nf}} = \frac{\mu_{\mathrm{bf}}}{(1-\varphi_1)^{2.5}}$	$\mu_{\mathrm{hnf}} = \frac{\mu_{\mathrm{bf}}}{(1-\varphi_1)^{2.5}(1-\varphi_2)^{2.5}}$
Density (ρ)	$\rho_{\mathrm{nf}} = (1-\varphi_1)\rho_{\mathrm{bf}} + \varphi_1\rho_{\mathrm{s1}}$	$\rho_{\mathrm{hnf}} = (1-\varphi_2)((1-\varphi_1)\rho_{\mathrm{bf}} + \varphi_1\rho_{\mathrm{s1}}) + \varphi_2\rho_{\mathrm{s2}}$
Heat capacity (ρc_{p})	$(\rho c_{\mathrm{p}})_{\mathrm{nf}} = (1-\varphi_1)(\rho c_{\mathrm{p}})_{\mathrm{bf}} + \varphi_1(\rho c_{\mathrm{p}})_{\mathrm{s1}}$	$(\rho c_{\mathrm{p}})_{\mathrm{hnf}} = (1-\varphi_2)\left((1-\varphi_1)(\rho c_{\mathrm{p}})_{\mathrm{bf}} + \varphi_1(\rho c_{\mathrm{p}})_{\mathrm{s1}}\right) + \varphi_2(\rho c_{\mathrm{p}})_{\mathrm{s2}}$
Thermal conductivity (k)	$\frac{k_{\mathrm{nf}}}{k_{\mathrm{bf}}} = \frac{k_{\mathrm{s1}}+2k_{\mathrm{bf}}-2\varphi_1(k_{\mathrm{bf}}-k_{\mathrm{s1}})}{k_{\mathrm{s1}}+2k_{\mathrm{bf}}+\varphi_1(k_{\mathrm{bf}}-k_{\mathrm{s1}})}$	$\frac{k_{\mathrm{hnf}}}{k_{\mathrm{nf}}} = \frac{k_{\mathrm{s2}}+2k_{\mathrm{nf}}-2\varphi_2(k_{\mathrm{nf}}-k_{\mathrm{s2}})}{k_{\mathrm{s2}}+2k_{\mathrm{nf}}+\varphi_2(k_{\mathrm{nf}}-k_{\mathrm{s2}})}$ where $k_{\mathrm{nf}} = k_{\mathrm{bf}}\left(\frac{k_{\mathrm{s1}}+2k_{\mathrm{bf}}-2\varphi_1(k_{\mathrm{bf}}-k_{\mathrm{s2}})}{k_{\mathrm{s1}}+2k_{\mathrm{bf}}+\varphi_1(k_{\mathrm{bf}}-k_{\mathrm{s2}})}\right)$

Table 2 Thermo-physical attributes of nano additives and ethylene glycol

Properties	Regular fluid	Nanoparticles		
	$C_2H_6O_2$	SWCNT	MWCNT	Fe_3O_4
? (kg m^3)	1115	2600	1600	5200
c_{p} (J/kg/K)	2430	425	796	670
k (W/m/K)	0.253	6600	3000	6

2.4 Similarity conversion

The following similarity transformations are used to get the non-dimensionalisation of Eqs. (11), (13) and (19).

$$\psi = \sqrt{\frac{2\vartheta_{\mathrm{bf}}\breve{x}\breve{u}_e}{m+1}}\, f(\xi), \xi = \sqrt{\frac{(m+1)\breve{u}_e}{2\vartheta_{\mathrm{bf}}\breve{x}}}\,\breve{y},\ \theta(\xi) = \frac{\breve{T}-\breve{T}_\infty}{\breve{T}_w-\breve{T}_\infty},\ \phi(\xi) = \frac{\breve{C}-\breve{C}_\infty}{\breve{C}_w-\breve{C}_\infty}, \tag{20}$$

here, ψ is the stream function that satisfies Eq. (10) with the velocities $\breve{u}$ and $\breve{v}$ as

$$\begin{aligned}\breve{u} = \frac{\partial\psi}{\partial\breve{y}} &= \breve{U}_\infty\breve{x}^m f'(\xi), \breve{v} = -\frac{\partial\psi}{\partial\breve{x}} \\ &= -\left[\sqrt{\frac{\vartheta_{bf}\breve{U}_\infty(m+1)}{2}}\breve{x}^{\left(\frac{m-1}{2}\right)}\left(f(\xi) + \xi\left(\frac{m-1}{m+1}\right)f'(\xi)\right)\right],\end{aligned} \tag{21}$$

by employing Eqs. (20) and (21), the Eqs. (11), (13), (14), (15) and (19) can be transmuted as

$$f'''\left[1-\frac{\mathrm{ReDe}}{6}\left(\frac{m+1}{2}\right)\left(f''\right)^{2}\right]^{n}$$
$$-\frac{n}{3}\mathrm{ReDe}\left(\frac{m+1}{2}\right)\left(f''\right)^{2}f'''\left[1-\frac{\mathrm{ReDe}}{6}\left(\frac{m+1}{2}\right)\left(f''\right)^{2}\right]^{n-1}$$
$$+\frac{\epsilon_2}{\epsilon_1}\left(\frac{2m}{m+1}\right)\left(1-f'^{2}\right)+\frac{\epsilon_2}{\epsilon_1}ff''+\epsilon_1\left(\frac{2}{m+1}\right)M\left(1-f'\right)=0, \tag{22}$$

$$\left(1+\frac{R_{\mathrm{d}}}{\epsilon_4}\right)\theta''+\mathrm{Pr}\frac{\epsilon_3}{\epsilon_4}\left(f\theta'+\mathrm{Nb}\theta'\phi'+\mathrm{Nt}\left(\theta'\right)^{2}\right)$$
$$+Pr\frac{\epsilon_1}{\epsilon_4}\mathrm{Ec}\left(f''\right)^{2}\left[1-\frac{\mathrm{ReDe}}{6}\left(\frac{m+1}{2}\right)\left(f'\right)^{2}\right]^{n}=0, \tag{23}$$

$$\phi'+\mathrm{Le}f\phi'+\frac{\mathrm{Nt}}{\mathrm{Nb}}\theta'-\mathrm{Le}\left(\frac{2\sigma}{m+1}\right)(1+\delta\theta)^{\breve{N}_0}\exp\left(\frac{-E}{1+\delta\theta}\right)\phi=0. \tag{24}$$

where $\epsilon_1=\frac{1}{(1-\varphi_1)^{2.5}(1-\varphi_2)^{2.5}}$, $\epsilon_2=(1-\varphi_2)\left[(1-\varphi_1)+\varphi_1\left(\frac{\rho_{\mathrm{s1}}}{\rho_{\mathrm{bf}}}\right)\right]+\varphi_2\left(\frac{\rho_{\mathrm{s2}}}{\rho_{\mathrm{bf}}}\right)$, $\epsilon_3=(1-\varphi_2)\left[(1-\varphi_1)+\varphi_1\left(\frac{(\rho c_{\mathrm{p}})_{\mathrm{s1}}}{(\rho c_{\mathrm{p}})_{\mathrm{bf}}}\right)\right]+\varphi_2\left(\frac{(\rho c_{\mathrm{p}})_{s2}}{(\rho c_{\mathrm{p}})_{\mathrm{bf}}}\right)$, $\epsilon_4=\frac{k_{\mathrm{hnf}}}{k_{\mathrm{bf}}}$.

The transmuted boundary conditions are

$$f=0,\ f'=\gamma,\theta=1,\phi=1\mathrm{at}\xi=0, \tag{25}$$

$$f'=1,\theta=0,\phi=0\mathrm{at}\xi\to\infty. \tag{26}$$

whereas the physical parameters associated Eqs. (22)–(24) and (25) are:

$M=\frac{\sigma_{\mathrm{bf}}B_0{}^2}{\rho_{\mathrm{bf}}\breve{U}_\infty}$(Magnetic parameter), $\gamma=\frac{\breve{U}_{\mathrm{w}}}{\breve{U}_\infty}$ (moving wedge parameter), $\mathrm{Re}=\frac{\breve{U}_\infty\breve{x}^{m+1}}{\vartheta_{\mathrm{bf}}}$ (Reynolds number), $\mathrm{De}=\breve{U}_\infty^{2}\widehat{\beta}_1^{2}\breve{x}^{2m}$ (Deborah number), $\mathrm{Pr}=\frac{\vartheta_{\mathrm{bf}}}{\alpha_{\mathrm{bf}}}$ (Prandtl number), $\mathrm{Nb}=\frac{D_{\mathrm{B}}\tau\left(\breve{C}_w-\breve{C}_\infty\right)}{\vartheta_{\mathrm{bf}}}$ (Brownian motion parameter), $\mathrm{Nt}=\frac{D_{\mathrm{T}}\tau\left(\breve{T}_w-\breve{T}_\infty\right)}{\vartheta_{\mathrm{bf}}\breve{T}_\infty}$ (thermophoresis parameter), $R_{\mathrm{d}}=\frac{16\sigma^*\breve{T}_\infty^{3}}{3k_{bf}k^*}$ (radiation parameter), $\mathrm{Ec}=\frac{\breve{U}_\infty^{2}\breve{x}^{2m}}{(c_p)_{bf}\left(\breve{T}_w-\breve{T}_\infty\right)}$ (Eckeret number), $\mathrm{Le}=\frac{\vartheta_{\mathrm{bf}}}{D_{\mathrm{B}}}$ (Lewis number), $\delta=\frac{\left(\breve{T}_w-\breve{T}_\infty\right)}{\breve{T}_\infty}$ (heat source parameter), $\sigma=\frac{k_0^2}{\breve{U}_\infty}$ (rate of a chemical reaction), $E=\frac{E_{\mathrm{a}}}{\kappa\breve{T}_\infty}$ (activation energy).

2.5 Physical quantities

The three key important physical quantities of this present analysis are as follows:

$$\breve{C}_{\mathrm{fx}}=\frac{\mu_{\mathrm{hnf}}\left[\left(\left(1-\frac{\hat{\beta}_1^2}{6}\left(\frac{\partial\breve{u}}{\partial\breve{y}}\right)^{2}\right)^{n}\left(\frac{\partial\breve{u}}{\partial\breve{y}}\right)\right]\right|_{\breve{y}=0}}{\rho u_{\mathrm{w}}^{2}}$$

$$= \frac{1}{(1-\varphi_1)^{2.5}(1-\varphi_2)^{2.5}}\sqrt{\frac{m+1}{2}}f''(0)\sqrt{\frac{1}{\mathrm{Re}}}\left[1-\frac{\mathrm{ReDe}}{6}\left(\frac{m+1}{2}\right)\left(f''(0)\right)^2\right]^n,$$

$$\breve{H}_{\mathrm{tx}} = \frac{\breve{x}\left[-k_{\mathrm{hnf}}\left.\frac{\partial \breve{T}}{\partial \breve{y}}\right|_{\breve{y}=0} - \frac{16\sigma^*}{3k^*}\left(\breve{T}_\infty^3\frac{\partial \breve{T}}{\partial \breve{y}}\right)\Big|_{\breve{y}=0}\right]}{k_{\mathrm{bf}}\left(\breve{T}_{\mathrm{w}}-\breve{T}_\infty\right)} = -\frac{k_{\mathrm{hnf}}}{k_{\mathrm{bf}}}\sqrt{\mathrm{Re}}\sqrt{\frac{m+1}{2}}[1+R_{\mathrm{d}}]\theta'(0),$$

$$\breve{N}t_x = \frac{-\breve{x}D_{\mathrm{B}}\left.\frac{\partial \tilde{C}}{\partial \breve{y}}\right|_{\breve{y}=0}}{D_{\mathrm{B}}\left(\breve{C}_{\mathrm{w}}-\breve{C}_\infty\right)} = -\sqrt{\mathrm{Re}}\sqrt{\frac{m+1}{2}}\varphi'(0). \tag{27}$$

where $\mathrm{Re} = \frac{\breve{u}_e\breve{x}}{\vartheta_{\mathrm{bf}}}$ exemplifies the local Reynolds number.

3 Methodology

3.1 Numerical simulation

The coupled nonlinear ODEs (22)–(24) with transmuted boundary conditions (25) and (26) are lessened to the first order system by using the following approach, which is further resolved through the shooting technique combined with RKF-45 integration scheme (Elayarani et al. 2021).

$$f = p_1, f' = p_2, f'' = p_3, \theta = q_1, \theta' = q_2, \phi = r_1, \phi' = r_2,$$

$$\begin{cases} f''' = p_3' = \dfrac{-\frac{\varepsilon_2}{\varepsilon_1}\left(\frac{2m}{m+1}\right)(1-p_2^2)-\frac{\varepsilon_2}{\varepsilon_1}p_1p_3-\varepsilon_1\left(\frac{2}{m+1}\right)M(1-p_2)}{\left(1-\frac{\mathrm{ReDe}}{6}\left(\frac{m+1}{2}\right)p_3^2\right)^n-\frac{n}{3}\mathrm{ReDe}\left(\frac{m+1}{2}\right)p_3^2\left(1-\frac{\mathrm{ReDe}}{6}\left(\frac{m+1}{2}\right)p_3^2\right)^{n-1}}, \\ \theta'' = q_2' = \dfrac{-\mathrm{Pr}\frac{\varepsilon_3}{\varepsilon_4}(p_1q_2+Nbq_2r_2+Ntq_2^2)-\mathrm{Pr}\frac{\varepsilon_1}{\varepsilon_4}Ecp_3^2\left(1-\frac{\mathrm{ReDe}}{6}\left(\frac{m+1}{2}\right)p_3^2\right)^n}{\left(1+\frac{R_d}{\varepsilon_4}\right)}, \\ \phi'' = r_2' = -\mathrm{Le}p_1r_2-\frac{\mathrm{Nt}}{\mathrm{Nb}}q_2'+\mathrm{Le}\left(\frac{2\sigma}{m+1}\right)(1+\delta q_1)^{\tilde{n}_0}\exp\left(\frac{-E}{1+\delta q_1}\right)r_1, \end{cases} \tag{28}$$

with the corresponding initial conditions

$$\left.\begin{array}{l} p_1 = 0, p_2 = \gamma, p_3 = \alpha_1, q_1 = 1, q_2 = \alpha_2, r_1 = 1, r_2 = \alpha_3 \text{ at } \xi = 0, \\ p_2 \to 1, q_1 \to 0, r_1 \to 0 \text{ as } \xi \to \infty. \end{array}\right\}. \tag{29}$$

To solve (28) and (29), initial guesses are formed for the unknown initial values α_1, α_2, and α_3, and numerical integration is accomplished using the Runge–Kutta–Fehlberg (RKF) fourth-fifth order integration scheme. When the computed values of $f'(\xi)$, $\theta(\xi)$ and $\phi(\xi)$ as $\xi \to \infty$ are compared with the specified boundary conditions $f'(\infty) = 1$, $\theta(\infty) = 0$ and $\phi(\infty) = 0$, the values of α_1, α_2, and α_3 are adjusted to obtain a better approximation, and the procedure is repeated until convergence with an error of $< 10^{-5}$ is obtained. The framework of the present flow model is presented in Fig. 2.

A comparison is made between the present results and previously published literature to verify the accuracy of our numerical scheme. Validation of numerical computations (RKF-45) of the friction coefficient (($\breve{C}_{fx}$) for various values of m is accomplished by comparing the

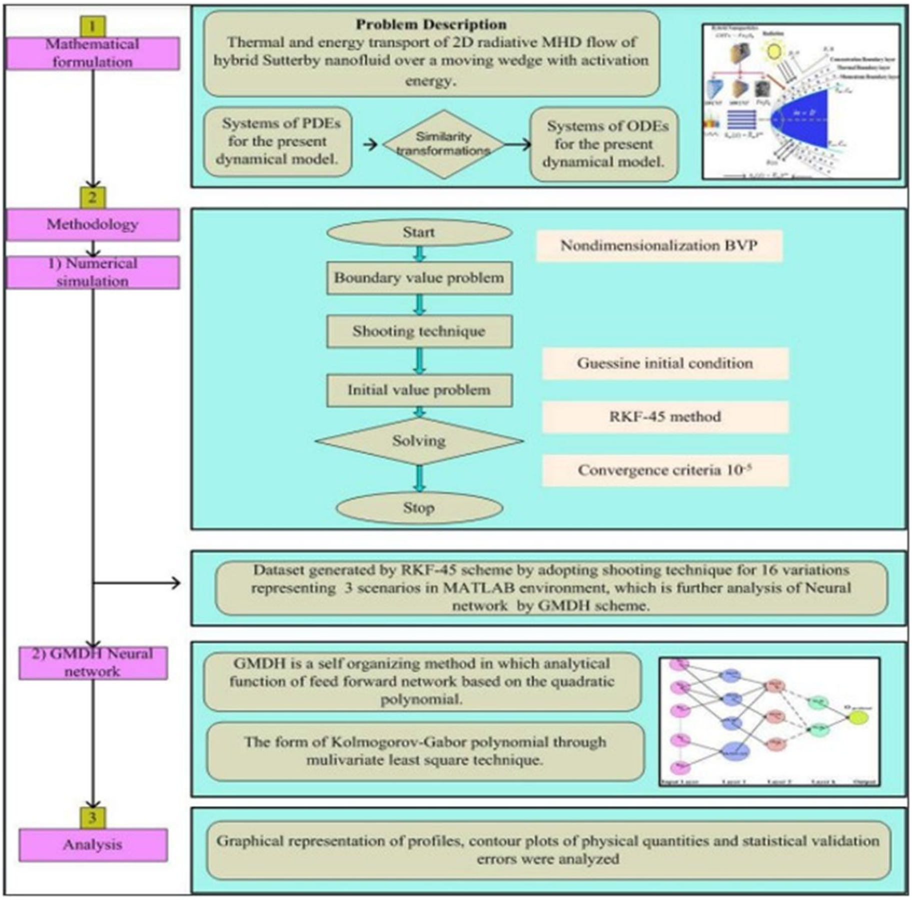

Fig. 2 Work flow diagram for the Sutterby hybrid nanofluid

results of the current investigations with those of Yacob et al. (2011) (Keller-box method), Gopi Krishna and Shanmugapriya (2021) (HPM method), and Tulu and Ibrahim (2019) (SQLM method) as shown in Tables 3. The calculated results of the friction factor are in good accord with the published results.

3.2 Group method of data handling

GMDH concept is related to the ANN model as a shape of the complicated human brain network represented by non-linear functions of a parallel acting approach. This network structure is a self-organizing method in which the behavior system is identified by evaluating its performance over a set of multi-input with respect to single-output data sets. This model constructs an analytical function of a feed-forward network based on the quadratic node transmission feature, whose coefficients are determined by a regression model. Using the GMDH algorithm, a model is visualized as a set of neurons over different sets thereby every layer is normally interconnected via a second-degree polynomial treated as neurons of the

Table 3 Comparison of $f^{\prime\prime}(0)$ when $M = \gamma = \mathrm{Re} = \mathrm{De} = \varphi_1 = \varphi_2 = n = 0$

m	Yacob et al. (2011) (Keller-box)	Gopi Krishna and Shanmugapriya (2021) (HPM)	Tulu and Ibrahim (2019) (SQLM)	Present results (RKF-45)
0	0.4696	0.4932	0.46960	0.4696
1/11	0.6550	0.6875	0.65498	0.6550
1/5	0.8021	0.8467	0.80213	0.8021
1/3	0.9277	0.9708	0.92768	0.9277
1/2	1.0389	1.0598	1.03907	1.0389
1	1.2326	1.1324	1.23258	1.2326

adjacent layer. These sorts of illustrations hired to map inputs area to outputs area. The general structure of the GMDH neural network is shown in Fig. 3. The functional prediction $\left(\widehat{F}\right)$ have to be done such that it could be utilized in preference to the actual (F) function. For a given input vector $S_I = (s_1, s_2, s_3, \ldots s_N)$ the predicted parameter $\left(\widehat{O}\right)$ value ought to be near the actual value of (O) (Harandizadeh et al. 2021). For that purpose, supplied L observations regarding multivariable input– single variable output data set:

$$O_i = F(s_{i1}, s_{i2}, s_{i3}, \ldots s_{iN}), (i = 1, 2, 3, \ldots, L). \tag{30}$$

The GMDH network is trained to categorise every input variable represented by

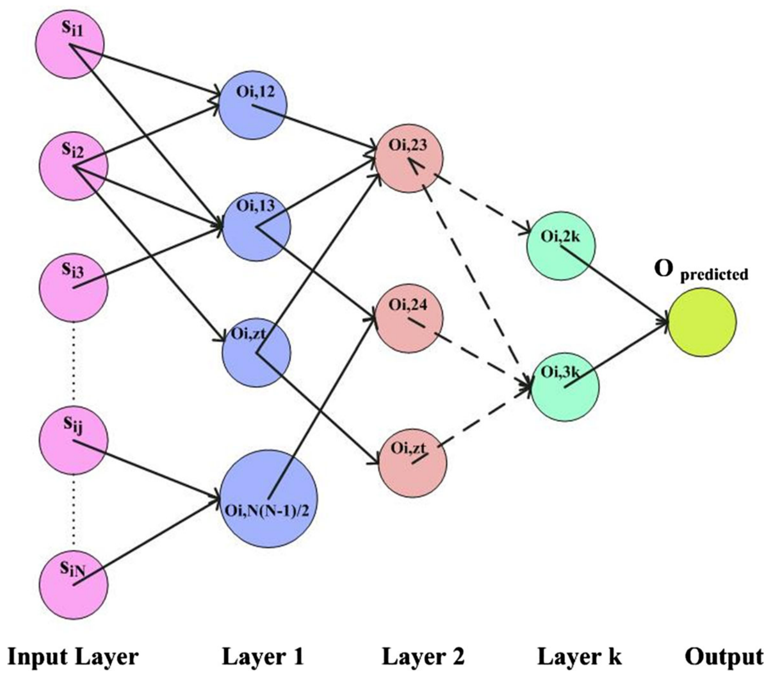

Fig. 3 General structure of GMDH model

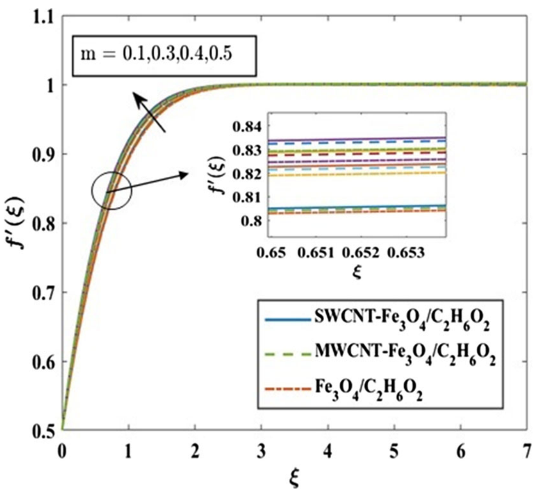

Fig. 4 Upshots of m on $f^{'}(\xi)$

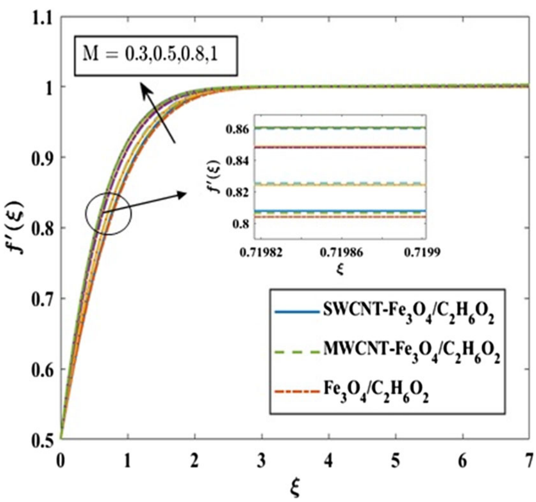

Fig. 5 Upshots of M on $f^{'}(\xi)$

$$\widehat{O_i} = \widehat{F}(s_{i1}, s_{i2}, s_{i3}, \ldots s_{iN}), (i = 1, 2, 3, \ldots, L). \tag{31}$$

The fundamental idea of this model ensures the minimum value that can be obtained from the difference between the predicted and actual values as given in the following

$$\sum_{i=1}^{L} \left[\widehat{F}(s_{i1}, s_{i2}, s_{i3}, \ldots s_{iN}) - O_i\right]^2 \rightarrow \text{Min} \tag{32}$$

The above expression is of the form Volterra–Kolmogorov–Gabor polynomial through GMDH model given by

$$O = b_0 + \sum_{i=1}^{N} b_i s_i + \sum_{i=1}^{N}\sum_{j=1}^{N} b_{ij} s_i s_j + \sum_{i=1}^{N}\sum_{j=1}^{N}\sum_{k=1}^{N} b_{ijk} s_i s_j s_k + \ldots. \tag{33}$$

Fig. 6 Upshots of Î^3 on $f^{'}(\xi)$

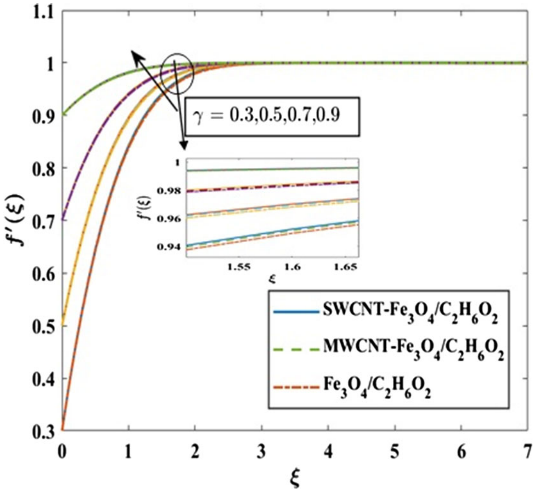

Fig. 7 Upshots of De on $f^{'}(\xi)$

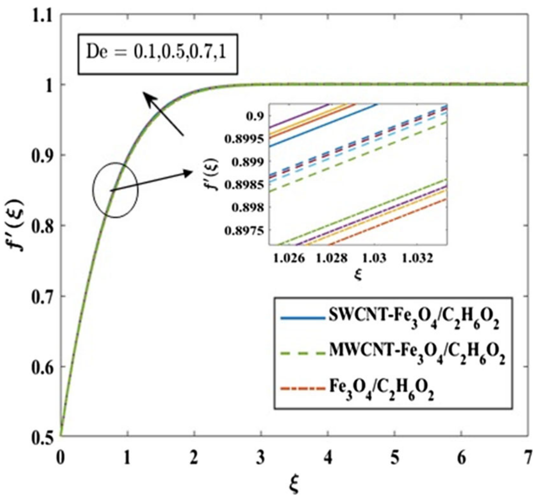

The shape of the mapping in every neuron is simplified using the output calculated from the pair of polynomials corresponding to the given data sets as

$$\widehat{O} = G\left(s_i, s_j\right) = b_0 + b_1 s_i + b_2 s_j + b_3 s_i s_j + b_4 {s_i}^2 + b_5 {s_j}^2 \tag{34}$$

where b_i ís are calculated from the pair of regression equations. The difference between the actual output O and predicted output $\widehat{O}$ for each s_i and s_j is minimized.

$$E_{\mathrm{r}} = \frac{1}{L}\sum_{i=1}^{L}\left(O_i - G\left(s_i, s_j\right)\right)^2 \rightarrow \text{Min.} \tag{35}$$

In GMDH method, to determine the coefficient for all above second order polynomials using a method of least square. Hence, the total of $\left(\frac{N}{2}\right) = \frac{N(N-1)}{2}$ neurons are made in the

Fig. 8 Upshots of Re on $f^{'}(\zeta)$

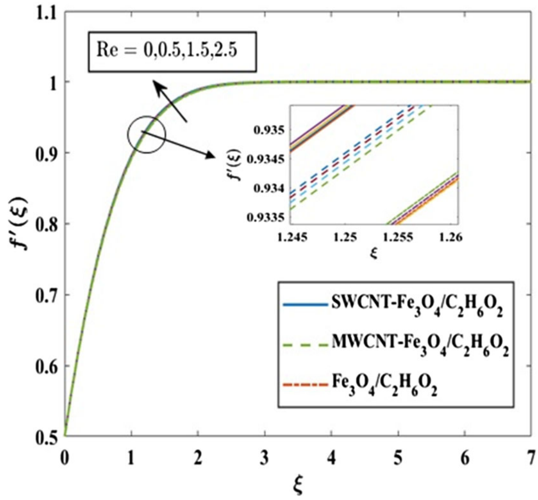

Fig. 9 Upshots of φ_1 on $\theta(\zeta)$

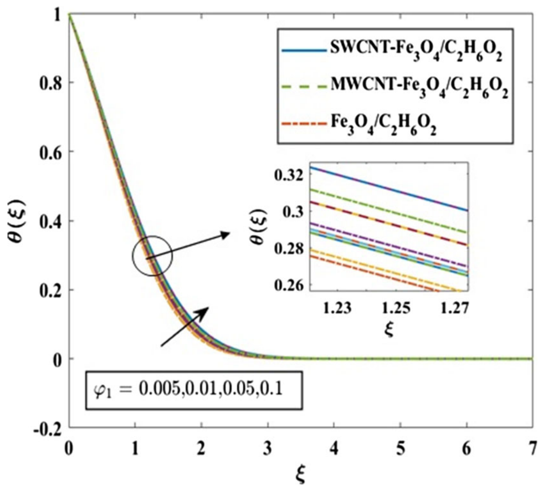

second layer of the network which could be expressed as below.

$$\{(O_i, s_{iz}, s_{it})/(i = 1, 2, 3, \ldots L)\&(z, t \in 1, 2, 3, \ldots, N)\}. \tag{36}$$

For a set of data points, the above Eq. (34) can be rewritten in matrix form

$$Ab = Y, \tag{37}$$

$$b = \{b_0, b_1, b_2, b_3, b_4, b_5\}, \tag{38}$$

$$Y = \{o_1, o_2, o_3, \ldots, o_L\}^{\mathrm{T}}, \tag{39}$$

Fig. 10 Upshots of φ_2 on $\theta(\xi)$

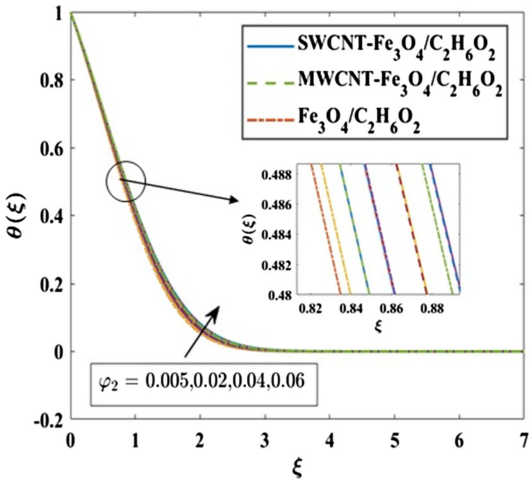

Fig. 11 Upshots of φ_1 on $\phi(\xi)$

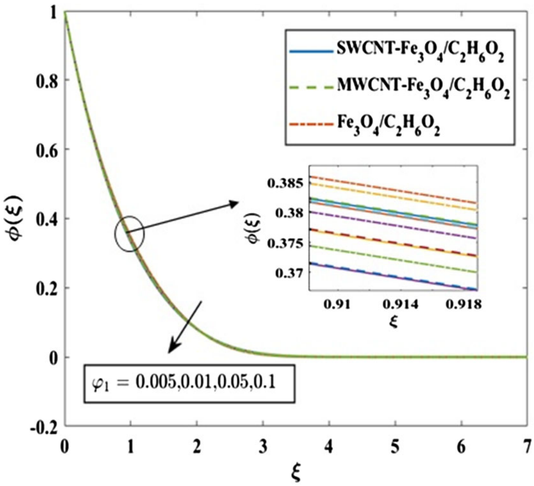

$$A = \begin{bmatrix} 1 & s_{1z} & s_{1t} & s_{1z}s_{1t} & {s_{1z}}^2 & {s_{1t}}^2 \\ 1 & s_{2z} & s_{2t} & s_{2z}s_{2t} & {s_{2z}}^2 & {s_{2t}}^2 \\ \dots & \dots & \dots & \dots & \dots & \dots \\ 1 & s_{Lz} & s_{Lt} & s_{Lz}s_{Lt} & {s_{Lz}}^2 & {s_{Lt}}^2 \end{bmatrix}. \tag{40}$$

Using the multivariate least square model, the co-efficients are determined as follows

$$b = \left(A^{\mathrm{T}}A\right)^{-1}A^{\mathrm{T}}Y. \tag{41}$$

This process is continued for each hidden neuron layer consisting of the GMDH network topology.

Fig. 12 Upshots of φ_2 on $\phi(\xi)$

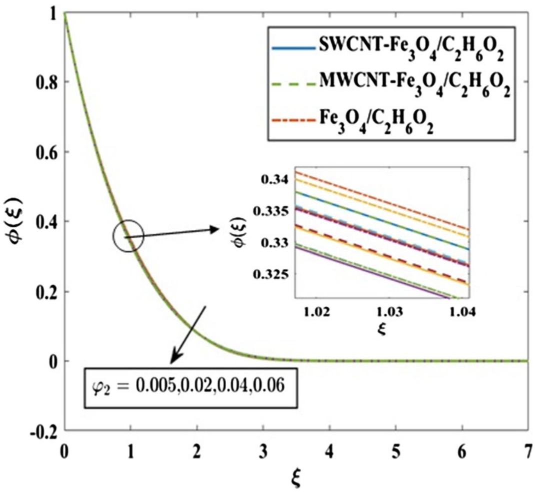

Fig. 13 Upshots of Nb on $\theta(\xi)$

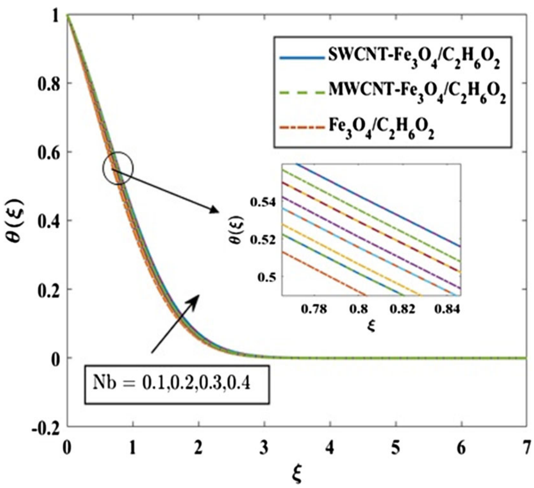

In this work, the GMDH models were constructed for predicting the skin friction ($\breve{C}_{fx}$), heat transfer rate $\left(\breve{H}_{tx}\right)$, and nanoparticle transfer rate (($\breve{N}t_x$) numbers. The numerical simulated input–output pairs (156 pairs) of data points with respect to the parameters such as m, Re, De, M, φ_1, φ_2, γ, Nb, Nt, R_d, Ec, Pr, Le, E, δ, σ and the corresponding output parameters $\breve{C}_{fx}$, $\breve{H}_{tx}$ and $\breve{N}t_x$ were employed for training the GMDH model. The data pairs were partitioned into two subsets, training (70%) and testing (30%) of the network. To estimate the performance of this model, the following standard statistical measures were used namely: mean square error (MSE), mean absolute error (MAE), root mean square error (RMSE) and coefficient of determination R^2 (Gopi Krishna et al. 2022).

$$\mathrm{MSE} = \frac{1}{N_\mathrm{ds}} \sum_{i=1}^{N_\mathrm{ds}} \left(T_i - \widehat{P}_i\right)^2. \tag{42}$$

Fig. 14 Upshots of Nb on $\phi(\xi)$

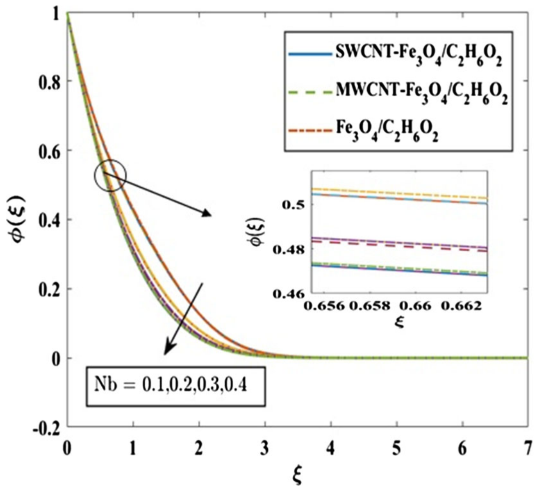

Fig. 15 Upshots of Nt on $\theta(\xi)$

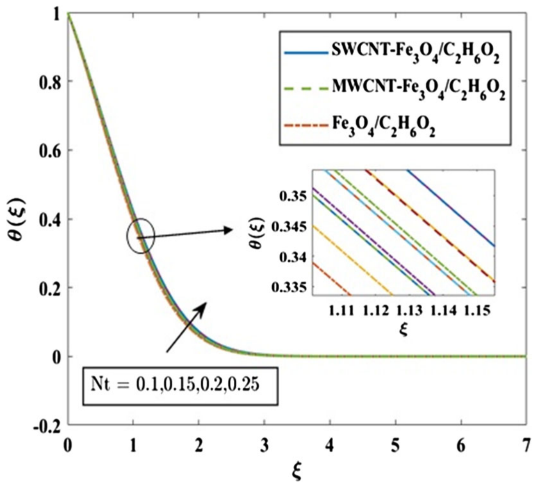

$$\text{MAE} = \frac{1}{N_{\text{ds}}} \sum_{i=1}^{N_{\text{ds}}} |T_i - \widehat{P}_i|. \tag{43}$$

$$\text{RMSE} = \sqrt{\frac{1}{N_{\text{ds}}} \sum_{i=1}^{N_{\text{ds}}} \left(T_i - \widehat{P}_i\right)^2}. \tag{44}$$

$$R^2 = 1 - \frac{\sum_{i=1}^{N_{\text{ds}}} \left(T_i - \widehat{P}_i\right)^2}{\sum_{i=1}^{N_{\text{ds}}} \left(T_i - \overline{T}\right)^2}. \tag{45}$$

$$\text{Errormean} = \frac{1}{N_{\text{ds}}} \sum_{i=1}^{N_{\text{ds}}} \left(T_i - \widehat{P}_i\right). \tag{46}$$

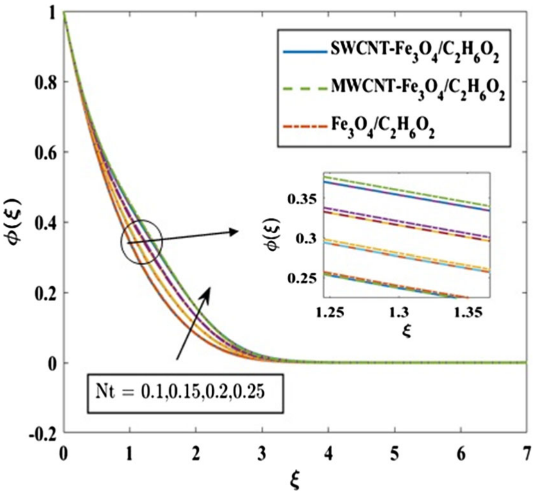

Fig. 16 Upshots of Nt on $\phi(\xi)$

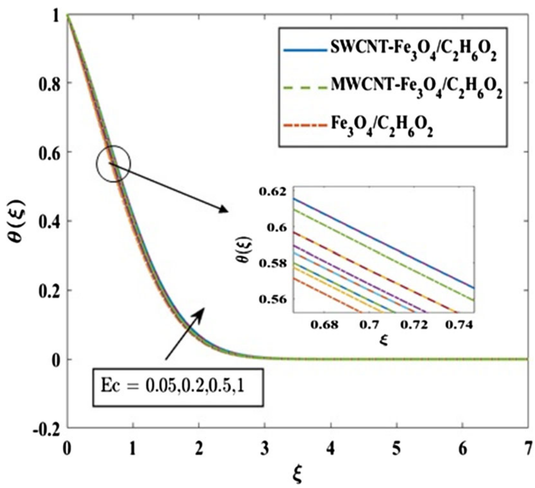

Fig. 17 Upshots of Ec on $\theta(\xi)$

$$\text{Errorstd} = \sqrt{\frac{1}{N_{\text{ds}} - 1} \sum_{i=1}^{N_{\text{ds}}} \left(E_i - \overline{E}\right)}. \tag{47}$$

here, N_{ds}, T_i, $\widehat{P_i}$, $\bar{T}$, E_i and $\overline{E}$ denotes the number of data set, specified target value, predicted value, average measure, actual measured value and the model outputs, respectively.

Fig. 18 Upshots of R_d on $\theta(\xi)$

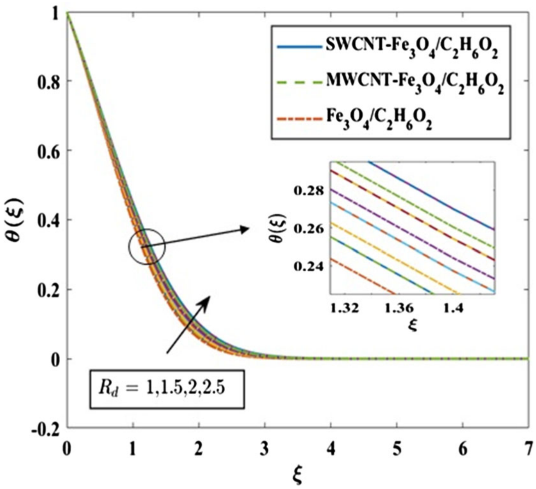

Fig. 19 Upshots of Le on $\phi(\xi)$

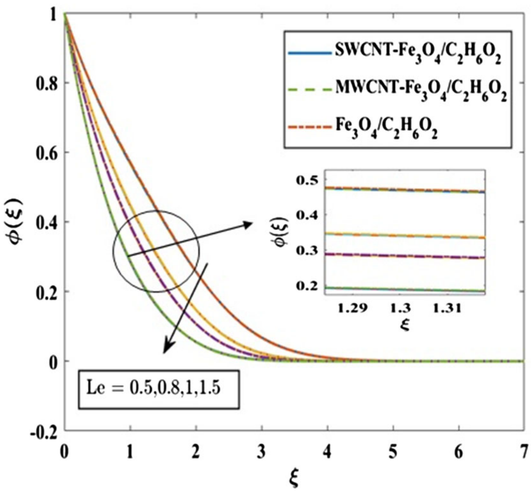

4 Results and discussion

4.1 Hydrodynamic and thermal boundary layers

In this portion, we have confined the graphical analysis of the sundry parameters versus involved profiles such as speed $\left(f^{'}(\xi)\right)$, thermal $(\theta(\xi))$, and focus $(\phi(\xi))$ for hybrid Sutterby nanofluid. Their outcomes are interpreted by Figs. 4, 5, 6, 7, 8, 9, 10, 11, 12, 13, 14, 15, 16, 17, 18, 19, 20, 21 and 22. It is illustrated the graphs on each parameter differ over some domain, and the remaining parameters have fixed the quantities $m = \mathrm{De} = \mathrm{Nt} = 0.1, \varphi_1 = \varphi_2 = 0.02, M = \gamma = \mathrm{Re} = \mathrm{Ec} = \delta = \sigma = 0.5, \mathrm{Nb} = 0.2, R_d = 1, E = 1, \mathrm{Le} = 1.2, \mathrm{Pr} = 6.2, n = 0.5$ and $\breve{N}_0 = 0.5$ for computational purpose. Comparative analysis of $(Fe_3O_4{-}C_2H_6O_2)$ nanofluid,

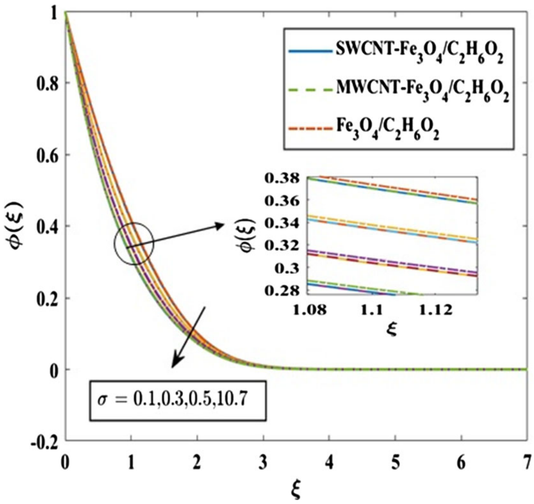

Fig. 20 Upshots of σ on $\phi(\xi)$

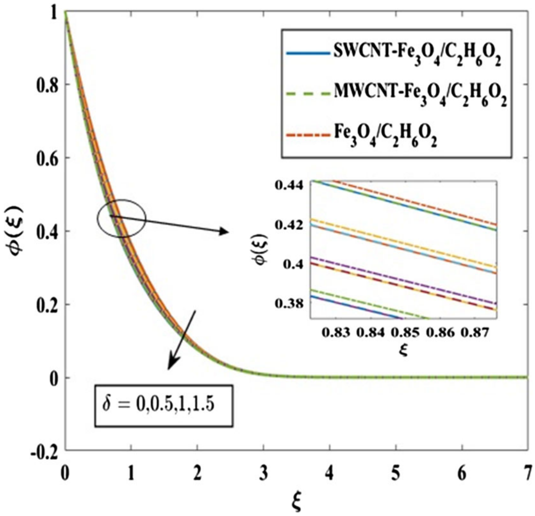

Fig. 21 Upshots of δ on $\phi(\xi)$

($SWCNT-Fe_3O_4/C_2H_6O_2$) and ($MWCNT-Fe_3O_4/C_2H_6O_2$) hybrid nanofluids are noticed and the effects of m, M, γ, DeandRe on $f^{'}(\xi)$ are depicted in Figs. 4, 5, 6, 7 and 8. The aftermath of m (Hartree parameter) on the velocity field is illustrated in Fig. 4. Growing values of m escalates $f^{'}(\xi)$. In general, increasing Hartree parameter m values exert more pressure on the flow, which tends to enhance the velocity field $f^{'}(\xi)$. Figure 5 visualizes the influence of M(magnetic parameter) on $f^{'}(\xi)$. It is discerned that rising values of M increases the velocity distributions of ($SWCNT-Fe_3O_4/C_2H_6O_2$), ($MWCNT-Fe_3O_4/C_2H_6O_2$) hybrid nanofluids and ($Fe_3O_4-C_2H_6O_2$) nanofluid. Physically, this occurs because of the reality that with amplifying the values of M, the Lorentz force raises, which elevates the retarding force to the movement of hybrid nanofluid CNTs and nanofluid Fe_3O_4. Variation of $f^{'}(\xi)$ with γ (moving wedge parameter) is captured in Fig. 6. It is depicted that $f^{'}(\xi)$ is enhanced for higher estimation of γ. As is well known, high values of γ causes more pressure to flow

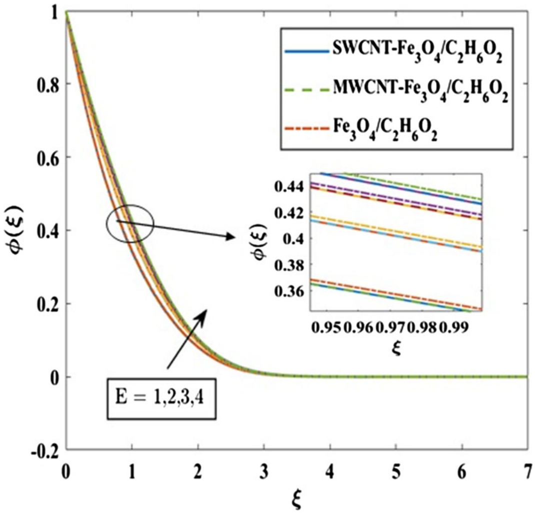

Fig. 22 Upshots of E on $\phi(\xi)$

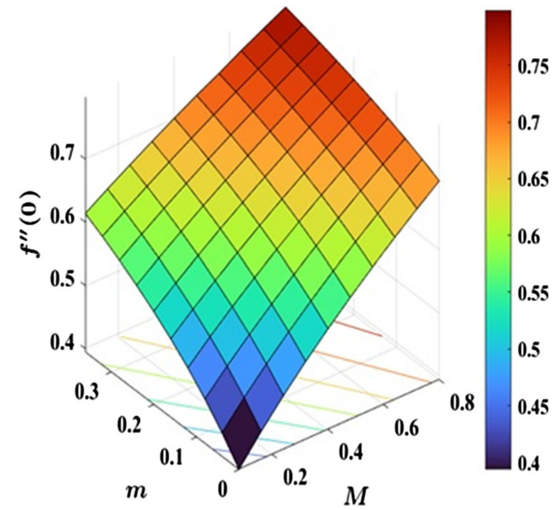

Fig. 23 Upshots of M and m on $f''(0)$ for $SWCNT-Fe_3O_4/C_2H_6O_2$

of velocity field. The consequence of De (Deborach number) on $f^{'}(\xi)$ is sketched in Fig. 7. It is perceived that, exaggerate of De lead to strengths of the velocity distribution $f^{'}(\xi)$. Scientifically, the Deborah number, which characterize the viscoelastic feature of the material is calculated as the proportion of the distinctive time to the time scale of deformation. The solidity of the material is greater with a higher Deborah number and for smaller values of Deborah number the fluidity increases. Hence, this validates that the augmentation in the Deborah number accelerates the fluid movement of the material. Figure 8 illuminates the influence of Re (Reynolds number) on $f^{'}(\xi)$. As Re elevates, the velocity distribution $f^{'}(\xi)$ upturns because the viscous force dominates the inertial force which cause a raises of fluid flow.

The effects of solid volume fraction $\varphi_1$of$Fe_3O_4$and$\varphi_2$ofCNTs on the thermal situation $\theta(\xi)$ and concentration $\phi(\xi)$ of $(Fe_3O_4-C_2H_6O_2)$ nanofluid, $(SWCNT-Fe_3O_4/C_2H_6O_2)$

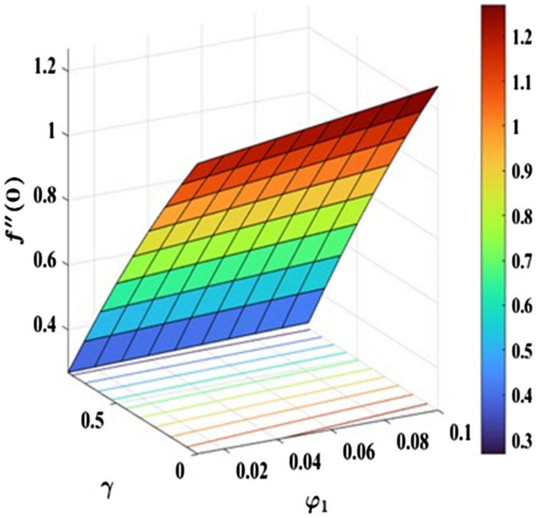

Fig. 24 Upshots of φ_1 and γ on $f''(0)$ for $SWCNT{-}Fe_3O_4/C_2H_6O_2$

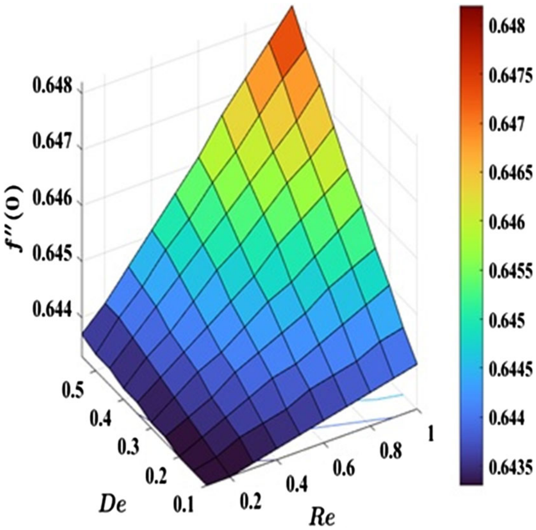

Fig. 25 Upshots of Re and De on $f''(0)$ for $SWCNT{-}Fe_3O_4/C_2H_6O_2$

and ($MWCNT{-}Fe_3O_4/C_2H_6O_2$) hybrid nanofluids are demonstrated in Figs. 9, 10, 11 and 12. By upsurge of $\varphi_1$andφ_2 in $C_2H_6O_2$, increase the temperature and decrease the concentration boundary layer thicknesses and hence $\theta(\xi)$ rises and $\phi(\xi)$ play down. The hybrid nanofluids ($CNTs{-}Fe_3O_4/C_2H_6O_2$) concentration leans to have smaller values as correlated to the ferrofluids, while hybrid nanoliquid ($CNTs{-}Fe_3O_4/C_2H_6O_2$) temperature distribution $\theta(\xi)$ is higher prominent. Figures 13, 14, 15 and 16 captured the significance of Nb and Nt (Browanian and thermophoresis parameter) on $\theta(\xi)$ and $\phi(\xi)$. From Figs. 13 and 14, highlights an augmented $\theta(\xi)$ for the growing strength of Nb, whereas decrementing behavior of $\phi(\xi)$ for raising Nb is noted. This by virtue of the zigzag movement and the colliding of macroscopic particles in fluid impairments with enhancing values of Nb. It is viewed from

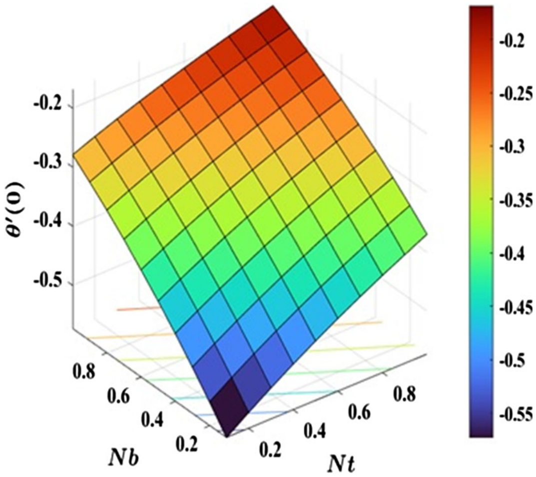

Fig. 26 Upshots of Nt and Nb on $\theta'(0)$ for $SWCNT{-}Fe_3O_4/C_2H_6O_2$

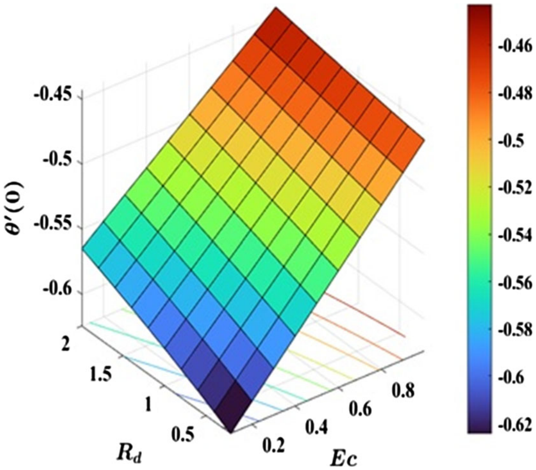

Fig. 27 Upshots of Ec and R_d on $\theta'(0)$ for $SWCNT{-}Fe_3O_4/C_2H_6O_2$

Figs. 15 and 16 that by enlarging the value of Nt there is raising in $\theta(\xi)$ and $\phi(\xi)$. This defines that the concentration profile and temperature get boosted through the departing of nano particles from a hot surface to a cold surface. Figure 17 renders the repercussion of Ec (Eckert number) on $\theta(\xi)$ of the CNTs and Fe_3O_4. With the augmentations of Ec, the temperature profile is $\theta(\xi)$ increases in the case of nanofluid Fe_3O_4 and hybrid nanofluid CNTs. Consequently, the production in Ec reinforces the kinetic energy due to which warmth boundary layer of nanoparticles intensifies. The impact of $\theta(\xi)$ of the nanofluid (Fe_3O_4) and hybrid nanofluid (CNTs) versus on R_d (Radiation parameter) is exhibited in Fig. 18. As raises in R_d indicates enhancement in the thermal field of nanoparticles Fe_3O_4 and hybrid nanoparticles CNTs. Therefore, the hybrid motion of the transportation power of solid nanomaterials of heat radiation is enhanced.

Figure 19 interprets the consequence of Le (Lewis number) on $\phi(\xi)$. As Le is heightended, the concentration distribution $\phi(\xi)$ is weakened because of the diffusivity of the mass degradation. Figure 20 inspects that the concentration distribution $\phi(\xi)$ tends to dwindling

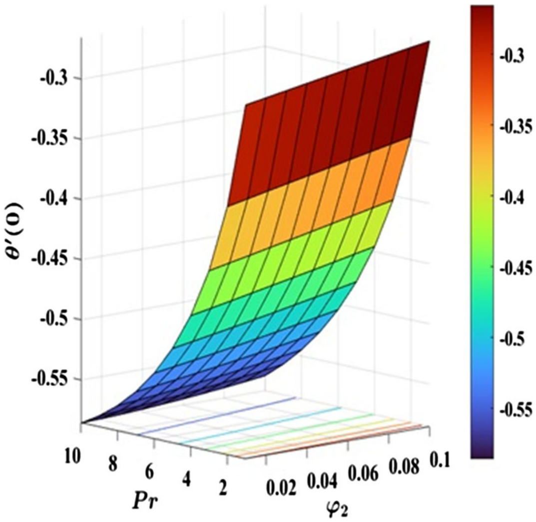

Fig. 28 Upshots of φ_2 and Pr on $\theta'(0)$ for $SWCNT-Fe_3O_4/C_2H_6O_2$

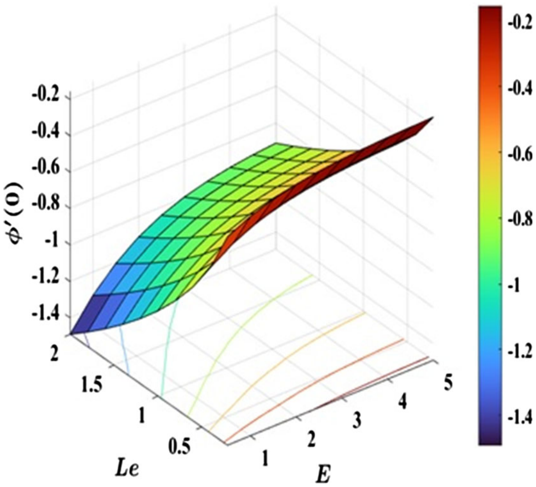

Fig. 29 Upshots of E and Le on $\phi'(0)$ for $Fe_3O_4/C_2H_6O_2$

on upsurging σ (dimensionless reaction rate). Substantially, improving values of σ leads to an enhance in the term.

$\sigma(1+\delta\theta)_0^{\overset{\smile}{N}}\exp\left(\frac{-E}{1+\delta\theta}\right)$ which contributes to catastrophic k_r (Chemical reaction rate) that reduces $\phi(\xi)$. The explanation for this behaviour is that the mass transfer rate is improved by the destructive chemical rate, which lowers the concentration of nanoparticles. These factors have an impact on the dampness and temperature destruction fields, resulting in the destruction of yields due to freezing, and causing vitality to typically move to the rainy cooling tower. Figure 21 shows that on account of amplifying δ, hybrid nanoparticles $(CNTs-Fe_3O_4/C_2H_6O_2)$ and nanoparticles $(Fe_3O_4/C_2H_6O_2)$ concentration $\phi(\xi)$ is abates. The impression of E (activation energy) in distribution of $\phi(\xi)$ is destroyed in Fig. 22. It is reveals that growing values of E leads to attained greatest level of $\phi(\xi)$. As a result the generative chemical reaction fall down. Therefore, as E augments, the concentration

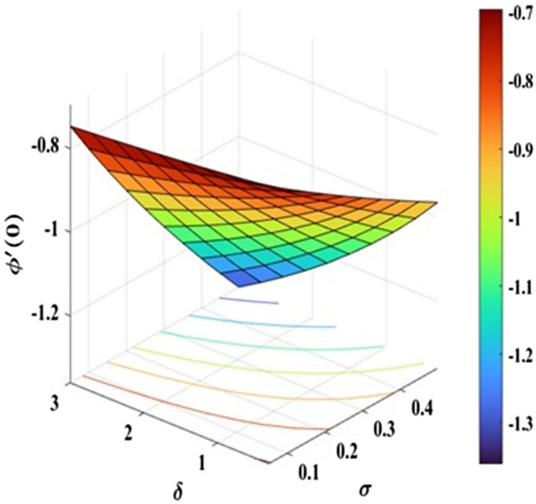

Fig. 30 Upshots of σ and δ on $\phi'(0)$ for $Fe_3O_4/C_2H_6O_2$

distribution $\phi(\xi)$ of the hybrid nanoparticles ($CNTs-Fe_3O_4/C_2H_6O_2$) and nanoparticles ($Fe_3O_4/C_2H_6O_2$) booms.

4.2 Surface contour plot analysis for physical interest

The 3D surface contour plots of three key important physical quantities such as friction factor $f''(0)$, rate of heat transport $\theta'(0)$ and rate of nonoparticle transport $\phi'(0)$ are explored in Figs. 23, 24, 25, 26, 27, 28, 29 and 30, respectively. Figure 23 depicts the consequence of $m$and$M$ on $f''(0)$ for ($SWCNT-Fe_3O_4/C_2H_6O_2$) hybrid nanofluid. The surface and contour plot inform that the growing values of m and M boosts the friction factor $f''(0)$ of hybrid nanofluid ($SWCNT-Fe_3O_4/C_2H_6O_2$). Figure 24 demenstrates the upshots of φ_1 and γ on $f''(0)$. The friction factor $f''(0)$ augments as φ_1 heightens, whereas the reverse upshot is seen on mounting γ. Figure 25 indicates the performance of Re and De on $f''(0)$. An enhance in Re and De strengthens the friction factor $f''(0)$. Figures 26, 27 and 28 elucidates the variations of heat transfer rate $\theta'(0)$ due to Nt, Nb, R_d, Ec, Pr and φ_2 via contour plots. It is perceived that on escalating Nt, Nb, R_d, Ec and φ_2 augments heat transfer rate, whereas, $\theta'(0)$ diminishes for growing Pr. The impression of mounting values of E, Le, σ and δ are deliberated in Figs. 29 and 30. An amplifying nature is exhibited by nonoparticle transfer rate $\phi'(0)$ on magnifying E, Le, σ and δ, however, $\phi'(0)$ reduces with growing values of σ and δ. As analysis of results, the friction factor and rate of heat transfer values are greater of hybrid nanoparticles ($SWCNT-Fe_3O_4/C_2H_6O_2$) than that of ($MWCNT-Fe_3O_4/C_2H_6O_2$) and ($Fe_3O_4/C_2H_6O_2$) nanofluid, while the nanoparticle transfer rate values are greater for nanofluid ($Fe_3O_4/C_2H_6O_2$) than that of ($CNTs-Fe_3O_4/C_2H_6O_2$) hybrid nanofluids.

Table 4 displays that the computational results of friction factor, rate of heat transport and rate of nanoparticle transport against various physical factors for ($SWCNT-Fe_3O_4/C_2H_6O_2$) hybrid Sutterby nanofluid. It is observed that the $\breve{C}_{fx} R_e^{0.5}$ and $\underset{tx}{\breve{H}} R_e^{-0.5}$ enhances the increasing values of φ_1, φ_2, m and M, also the $\breve{N}\, t_x R_e^{-0.5}$ are reduced as an augmentation of M, σ, δ, Nb and Le for ($SWCNT-Fe_3O_4/C_2H_6O_2$) hybrid nanofluid. The recogition that $\breve{C}_{fx} R_e^{0.5}$

Table 4 Outcomes of $\breve{C}_{fx} R_e^{0.5}$, $\breve{H}_{tx} R_e^{-0.5}$ and $\breve{N} t_x R_e^{-0.5}$ versus flow parameters

φ_1	φ_2	De	Re	m	M	γ	Nb	Nt	R_d	σ	δ	E	Le	$\breve{C}_{fx} R_e^{0.5}$	$\breve{H}_{tx} R_e^{-0.5}$	$\breve{N} t_x R_e^{-0.5}$
0.005														0.6353	− 0.5394	− 1.0021
0.01														0.6381	− 0.5372	− 1.003
0.05														0.6598	− 0.5194	− 1.0103
0.1														0.6863	− 0.4964	− 1.0195
	0.005													0.6423	− 0.5364	− 1.0043
	0.02													0.6436	− 0.5328	− 1.0049
	0.04													0.6464	− 0.5276	− 1.0059
	0.06													0.6505	− 0.522	− 1.0072
		0.1												0.6436	− 0.5328	− 1.0049
		0.5												0.6454	− 0.5329	− 1.005
		0.7												0.6463	− 0.533	− 1.0051
		1												0.6477	− 0.5331	− 1.0052
			0											0.6432	− 0.5327	− 1.0048
			0.5											0.6436	− 0.5328	− 1.0049
			1.5											0.6445	− 0.533	− 1.005
			2.5											0.6454	− 0.5331	− 1.0051
				0.1										0.6436	− 0.5328	− 1.0049
				0.3										0.7115	− 0.5299	− 0.9643
				0.4										0.7365	− 0.5287	− 0.9479
				0.5										0.7577	− 0.5276	− 0.9334
					0.3									0.5706	− 0.5362	− 0.998

Table 4 (continued)

φ_1	φ_2	De	Re	m	M	γ	Nb	Nt	R_d	σ	δ	E	Le	$\breve{C}_{fx} R_e^{0.5}$	$\breve{H}_{tx} R_e^{-0.5}$	$\breve{N}_{tx} R_e^{-0.5}$
					0.5									0.6436	− 0.5328	− 1.0049
					0.8									0.7407	− 0.5272	− 1.0139
					1									0.7992	− 0.5233	− 1.0193
						0.3								0.8713	− 0.4177	− 1.0094
						0.5								0.6436	− 0.5328	− 1.0049
						0.7								0.3986	− 0.6256	− 1.0086
						0.9								0.1369	− 0.6932	− 1.0221
							0.1							0.6436	− 0.5732	− 0.9238
							0.2							0.6436	− 0.5328	− 1.0049
							0.3							0.6436	− 0.4945	− 1.0319
							0.4							0.6436	− 0.4581	− 1.0454
								0.1						0.6436	− 0.5328	− 1.0049
								0.15						0.6436	− 0.5199	− 0.9883
								0.2						0.6436	− 0.5072	− 0.9761
								0.25						0.6436	− 0.4949	− 0.9681
									1					0.6436	− 0.5328	− 1.0049
									1.5					0.6436	− 0.5214	− 1.0072
									2					0.6436	− 0.5106	− 1.0094
									2.5					0.6436	− 0.5004	− 1.0115
										0.1				0.6436	− 0.5396	− 0.7385
										0.3				0.6436	− 0.5359	− 0.8779

Table 4 (continued)

φ_1	φ_2	De	Re	m	M	γ	Nb	Nt	R_d	σ	δ	E	Le	$\breve{C}_{fx} R_e^{0.5}$	$\breve{H}_{tx} R_e^{-0.5}$	$\breve{N}t_x R_e^{-0.5}$
										0.5				0.6436	− 0.5328	− 1.0049
										0.7				0.6436	− 0.5301	− 1.1218
											0			0.6436	− 0.5348	− 0.8985
											0.5			0.6436	− 0.5328	− 1.0049
											1			0.6436	− 0.5311	− 1.0962
											1.5			0.6436	− 0.5297	− 1.1752
												1		0.6436	− 0.5328	− 1.0049
												2		0.6436	− 0.5372	− 0.837
												3		0.6436	− 0.5396	− 0.749
												4		0.6436	− 0.5407	− 0.705
													0.5	0.6436	− 0.5548	− 0.588
													0.8	0.6436	− 0.5427	− 0.7929
													1	0.6436	− 0.5371	− 0.9051
													1.5	0.6436	− 0.5277	− 1.1379

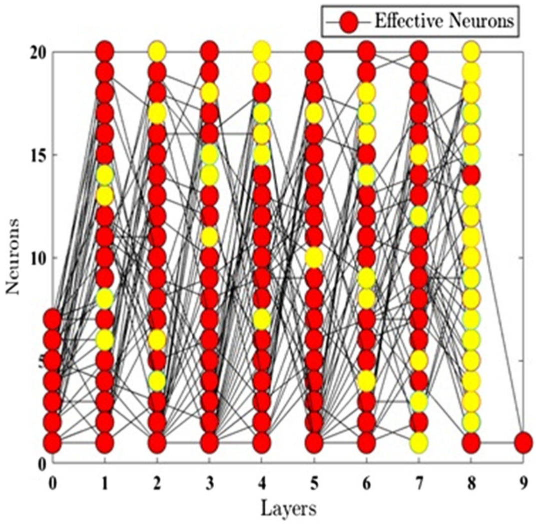

Fig. 31 Structure of evolved for GMDH model in $f''(0)$

improves the amplitude of Re and De, and boosting $\breve{H}_{tx} R_e^{-0.5}$ with the rises of Nt, Nb, and R_d. Further, the rate of nanoparticle transport $\breve{N}\, t_x R_e^{-0.5}$ enhances with growing values of E and Nt for $(\mathrm{SWCNT{-}Fe_3O_4/C_2H_6O_2})$ hybrid nanofluid.

4.3 Prediction GMDH model evaluation

The GMDH model is designed using the effective parameters, namely the number of layers, the number of neurons, and the selection pressure. The selection pressure factor enables the system to select the best fit for each stage and move it to the next layer. This process is repeated until it's reached the minimum error. A GMDH model of ten layers with twenty neurons, and 60% selection pressure has been developed and tested to determine its best performance. The evolved structure of GMDH models on $f''(0)$, $\theta'(0)$ and $\phi'(0)$ as shown in Figs. 31, 32 and 33. It can be observed that the first two outputs of $f''(0)$ and $\theta'(0)$ contain 9 hidden layers, while the third output $\phi'(0)$ contains 10 hidden layers.

The outcomes of the efficiency analysis of GMDH prognosis outputs for training and testing sets are epitomized in Table 5. The lower MAE error values and bigger R values of training and testing sets disport the conduct of the GMDH models. The curves between the numerical and predicted outputs for training and testing phases with statistical performance including RMSE, MSE, Error mean, and Error StD on $f''(0)$, $\theta'(0)$ and $\phi'(0)$ are illustrated in Figs. 34, 35 and 36. As shows that the errors RMSE, MSE, Error mean and Error StD attain the smallest values of the $f''(0)$, $\theta'(0)$ and $\phi'(0)$ outputs.

Figures 37, 38 and 39 exhibit the simulated versus predicted values of $f''(0)$,$\theta'(0)$ and $\phi'(0)$ for training and testing data sets. In this figure, the symmetrical straight lines are numerical values and the predicted values are represented near and far away from the straight lines. The numerical and the predicted values of the GMDH models are in good correlated with an error less than 3%.

Fig. 32 Structure of evolved for GMDH model in $\theta'(0)$

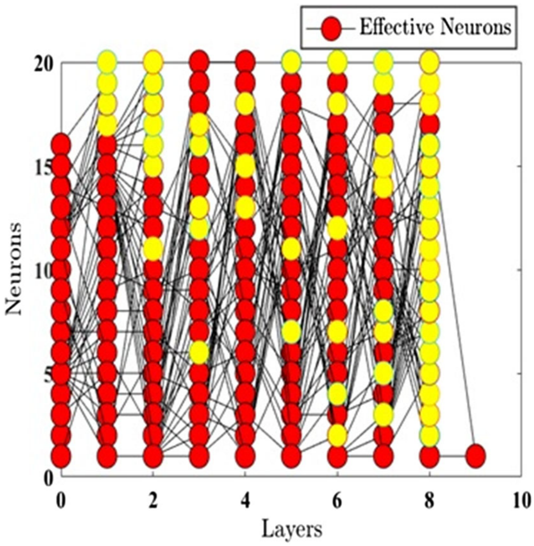

Fig. 33 Structure of evolved for GMDH model in $\phi'(0)$

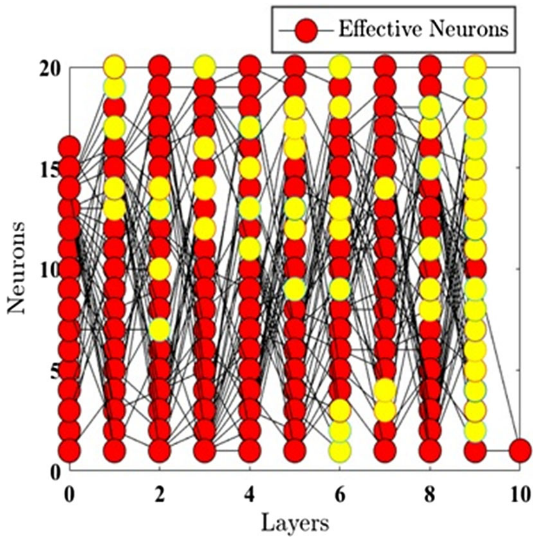

Table 5 Efficiency appraises of the established GMDH models for training and testing data sets

Data sets	Friction factor $\left(\breve{C}_{fx}\right)$		Rate of heat transfer $\left(\breve{H}_{tx}\right)$		Nanoparticle transfer rate $\left(\breve{N}t_x\right)$	
	MAE	R	MAE	R	MAE	R
Training	0.000198	1	0.004172	0.98363	0.004026	0.9959
Testing	4.68Eâ˘12	1	0.00155	0.99191	0.004513	0.99847

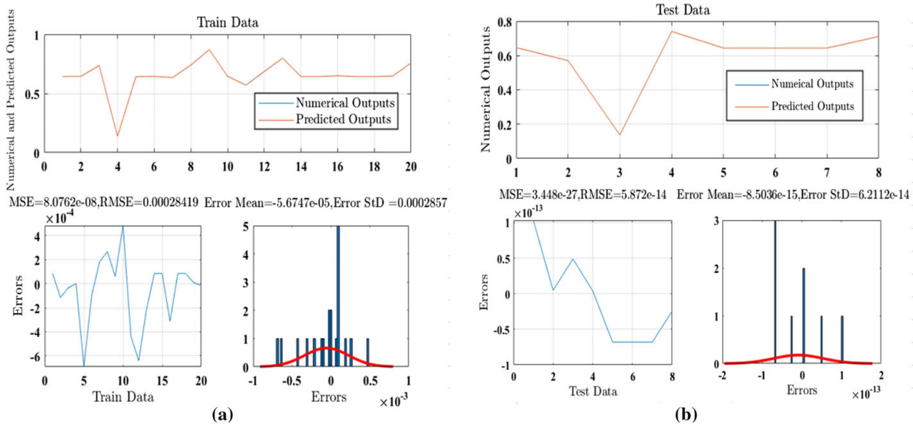

Fig. 34 The statistical validation errors with numerical versus predicted values of $f''(0)$ (**a**) training stage (**b**) testing stage

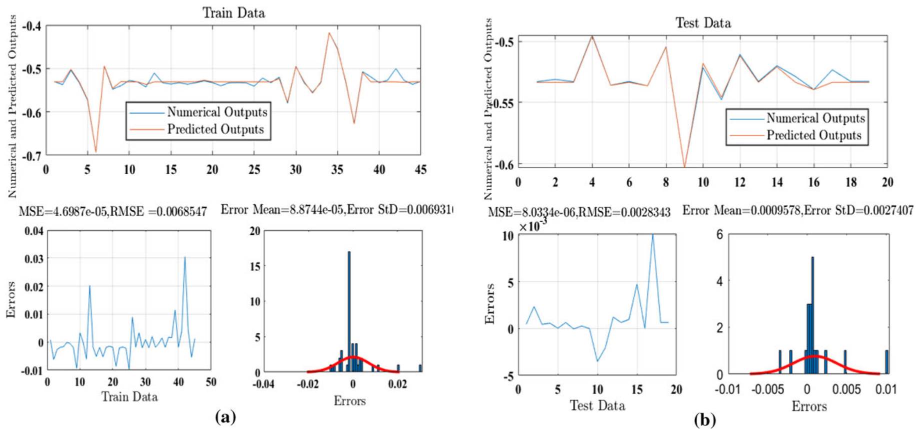

Fig. 35 The statistical validation errors with numerical versus predicted values of $\theta'(0)$ (**a**) training stage (**b**) testing stage

5 Concluding remarks

In this article, a radiative magnetohydrodynamic flow of hybrid Sutterby nanofluid past a moving wedge with activation energy has been investigated. The GMDH models were developed to predict the friction coefficient $((\breve{C}_{fx})$, heat transfer rate $\left(\breve{H}_{tx}\right)$, and nanoparticle transfer rate $((\breve{N}t_x)$. The core allegations of this analysis are pointed out as follows:

- $\theta(\xi)$ escalates and $\phi(\xi)$ degrades by enhance φ_1 and φ_2 for both Fe_3O_4 and CNTs. Furthermore, the concentration distribution is greater in $(Fe_3O_4/C_2H_6O_2)$ nanofluids than the $(CNTs{-}Fe_3O_4/C_2H_6O_2)$ hybrid nanofluids, whereas SWCNTs emerge to have a greater impact of temperature distribution $\theta(\xi)$ than MWCNTs.
- $f'(\xi)$ upgrades via m, M, γ, De and Re.

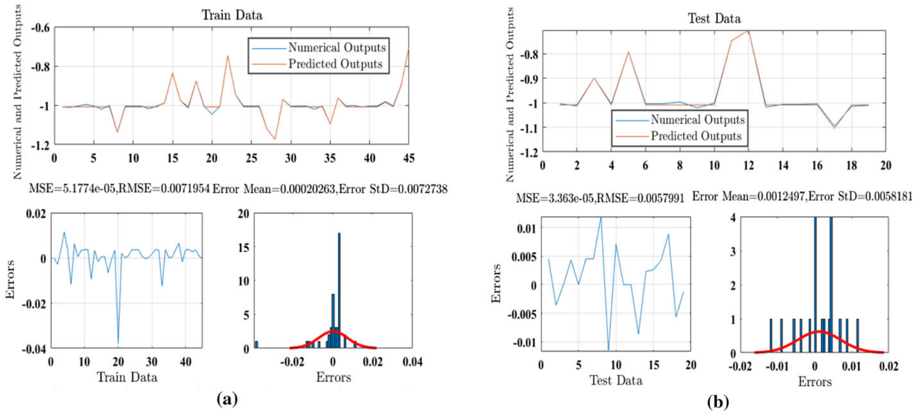

Fig. 36 The statistical validation errors with numerical versus predicted values of $\phi'(0)$ (**a**) training stage (**b**) testing stage

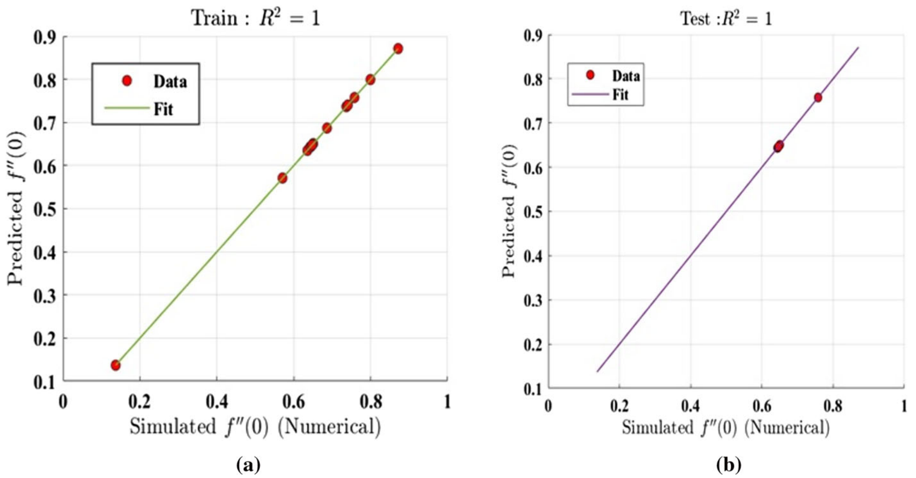

Fig. 37 Simulated versus predicted $f''(0)$ **a** training stage, **b** testing stage

- Growing of R_{d} and Ec intensifies $\theta(\xi)$.
- $\phi(\xi)$ proliferates by higher Nt and it diminish Nb.
- Improvement of E leads to upswing $\phi(\xi)$ and enlargement of Le, σ and δ decay $\phi(\xi)$.
- The friction factor $((\breve{C}_{fx})$ enhances with higher values of φ_1, Re and De for $(SWCNT{-}Fe_3O_4/C_2H_6O_2)$ hybrid nanofluid.
- The rate of heat transfer $(\breve{H}_{tx})$ magnifies by fluctuating φ_2 and R_d for $(SWCNT{-}Fe_3O_4/C_2H_6O_2)$ hybrid nanofluid, while the mass transfer rate $(\breve{N}_{tx})$ abatements due to Le, σ and δ.
- Hybrid nanofluids $(CNTs - Fe_3O_4/C_2H_6O_2)$ are the fatest agents for the analysis of thermal transport compared to regular fluids, and this nanoparticle recommented for the cooling equipment in the engineering applications.

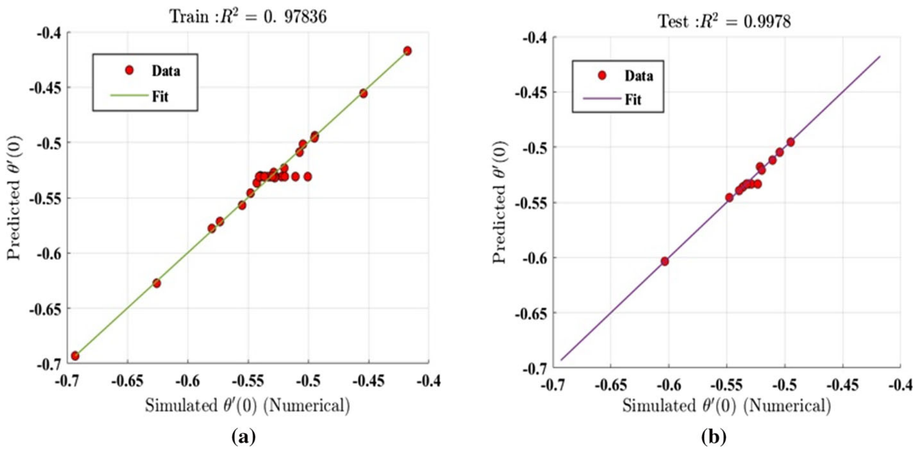

Fig. 38 Simulated versus predicted $\theta'(0)$ **a** training stage, **b** testing stage

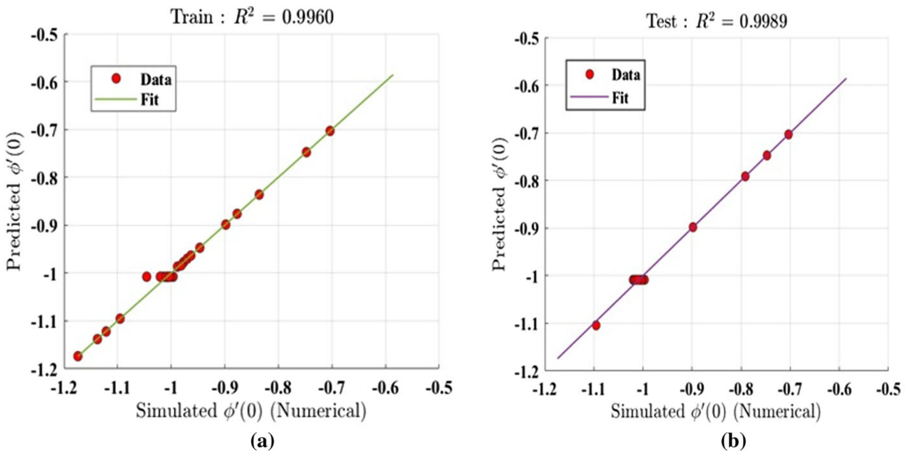

Fig. 39 Simulated versus predicted $\phi'(0)$ **a** training stage, **b** testing stage

- The coefficient of determination R^2, RMSE, MSE, Error mean and Error std diagrams and MRE values display the outcomes achieved from the GMDH models are in excellent concord with the numerical technique having an errors less than 3%.
- The GMDH models technique is accurate preditable with high efficiency for the thermal and energy transportation flow of a hybrid Sutterby nanofluid.

Acknowledgements The authors wish to thank the anonymous reviewers (Saeed et al. 2021; Bestman 1990).

Author contributions SGK conceived of the presented idea. MS prepared the manuscript and developed the theory and performed the computations. AA verified the analytical methods. AA investigated and supervised the findings of this work. All authors jointly worked on the results and they read and approved the final manuscript.

Funding This research did not receive any specific grant.

Availability of data and material All the data and material used in this research are included in the paper.

Declarations

Conflict of interest The authors declare that they have no competing interests.

References

Ali A, Jana RN, Das S (2021) Radiative CNT-based hybrid magneto-nanoliquid flow over an extending curved surface with slippage and convective heating. Heat Transfer 50(3):2997–3020

Ameen I, Shah Z, Islam S, Nasir S, Khan W, Kumam P, Thounthong P (2019) Hall and ion-slip effect on CNTS nanofluid over a porous extending surface through heat generation and absorption. Entropy 21(8):801

Amer Qureshi M (2021) Numerical simulation of heat transfer flow subject to MHD of Williams on nanofluid with thermal radiation. Symmetry 13(1):10

Atashrouz S, Rahmani M (2020) Predicting hydrogen storage capacity of metal–organic frameworks using group method of data handling. Neural Comput Appl 32(18):14851–14864

Ayub A, Sabir Z, Le DN, Aly AA (2021) Nanoscale heat and mass transport of magnetized 3-D chemically radiative hybrid nanofluid with orthogonal/inclined magnetic field along rotating sheet. Case Stud Thermal Eng 26:101193

Besthapu P, Haq RU, Bandari S, Al-Mdallal QM (2019) Thermal radiation and slip effects on MHD stagnation point flow of non-Newtonian nanofluid over a convective stretching surface. Neural Comput Appl 31(1):207–217

Bestman AR (1990) Natural convection boundary layer with suction and mass transfer in a porous medium. Int J Energy Res 14(4):389–396

Bilal M, Arshad H, Ramzan M, Shah Z, Kumam P (2021) Unsteady hybrid-nanofluid flow comprising ferrousoxide and CNTs through porous horizontal channel with dilating/squeezing walls. Sci Rep 11(1):1–16

Choi SU, Eastman JA (1995) Enhancing thermal conductivity of fluids with nanoparticles, vol 231. ASME-Publications-FED, San Francisco, pp 99–105

Elayarani M, Shanmugapriya M, Senthil Kumar P (2019) Estimation of magnetohydrodynamic radiative nanofluid flow over a porous non-linear stretching surface: application in biomedical research. IET Nanobiotechnol 13(9):911–922

Elayarani M, Shanmugapriya M, Senthil Kumar P (2021) Intensification of heat and mass transfer process in MHD carreau nanofluid flow containing gyrotactic microorganisms. Chem Eng Process Process Intensif 160:108299

Fathi S, Yazdi ME, Adamian A (2020) Estimation of contact heat transfer between curvilinear contacts using inverse method and group method of data handling (GMDH)-type neural networks. Heat Mass Transf 56:1–10

Fayyadh MM, Naganthran K, Basir MFM, Hashim I, Roslan R (2020) Radiative MHD Sutterby nanofluid flow past a moving sheet. Scaling group analysis. Mathematics 8(9):1430

Ferdows M, Shamshuddin MD, Salawu SO, Zaimi K (2021) Numerical simulation for the steady nanofluid boundary layer flow over a moving plate with suction and heat generation. SN Appl Sci 3(2):1–11

Ghadikolaei SS, Hosseinzadeh K, Hatami M, Ganji DD, Armin M (2018) Investigation for squeezing flow of ethylene glycol (C2H6O2) carbon nanotubes (CNTs) in rotating stretching channel with nonlinear thermal radiation. J Mol Liq 263:10–21

Ghosh S, Mukhopadhyay S (2020) Stability analysis for model-based study of nanofluid flow over an exponentially shrinking permeable sheet in presence of slip. Neural Comput Appl 32(11):7201–7211

Gopi Krishna S, Shanmugapriya M (2021) Inquiry of MHD bioconvective non-Newtonian nanofluid flow over a moving wedge using HPM. Mater Today Proc 38:3297–3305

Gopi Krishna S, Shanmugapriya M, Senthil Kumar P (2022) Prediction of bio-heat and mass transportation in radiative MHD Walter-B nanofluid using MANFIS model. Math Comput Simul 201:49–67

Gul T, Bilal M, Shuaib M, Mukhtar S, Thounthong P (2020) Thin film flow of the water-based carbon nanotubes hybrid nanofluid under the magnetic effects. Heat Transfer 49(6):3211–3227

Haider SMA, Ali B, Wang Q, Zhao C (2021) Stefan blowing impacts on unsteady mhd flow of nanofluid over a stretching sheet with electric field, thermal radiation and activation energy. Coatings 11(9):1048

Harandizadeh H, Jahed Armaghani D, Khari M (2021) A new development of ANFIS–GMDH optimized by PSO to predict pile bearing capacity based on experimental datasets. Eng Comput 37(1):685–700

Hayat T, Ayub S, Alsaedi A, Tanveer A, Ahmad B (2017) Numerical simulation for peristaltic activity of Sutterby fluid with modified Darcy's law. Results Phys 7:762–768

Hayat T, Qayyum S, Shehzad SA, Alsaedi A (2019a) Magnetohydrodynamic three-dimensional nonlinear convective flow of viscoelastic nanofluid with heat and mass flux conditions. Neural Comput Appl 31(4):967–977

Hayat T, Haider F, Muhammad T, Ahmad B (2019b) Darcy-Forchheimer flow of carbon nanotubes due to a convectively heated rotating disk with homogeneous–heterogeneous reactions. J Therm Anal Calorim 137(6):1939–1949

Ivakhnenko AG (1971) Polynomial theory of complex systems. IEEE Trans Syst Man Cybern 4:364–378

Jana S, Salehi-Khojin A, Zhong WH (2007) Enhancement of fluid thermal conductivity by the addition of single and hybrid nano-additives. Thermochim Acta 462(1–2):45–55

Jusoh R, Nazar R, Pop I (2019) Magnetohydrodynamic boundary layer flow and heat transfer of nanofluids past a bidirectional exponential permeable stretching/shrinking sheet with viscous dissipation effect. J Heat Transfer 141:012406

Khan MI, Qayyum S, Hayat T, Alsaedi A (2019) Stratified flow of Sutterby fluid with homogeneous-heterogeneous reactions and Cattaneo-Christov heat flux. Int J Numer Meth Heat Fluid Flow 29(8):2977–2992

Khan U, Shafiq A, Zaib A, Wakif A, Baleanu D (2020) Numerical exploration of MHD Falkner-Skan-Sutterby nanofluid flow by utilizing an advanced non-homogeneous two-phase nanofluid model and non-Fourier heat-flux theory. Alex Eng J 59(6):4851–4864

Khan WA, Anjum N, Waqas M, Abbas SZ, Irfan M, Muhammad T (2021a) Impact of stratification phenomena on a nonlinear radiative flow of Sutterby nanofluid. J Market Res 15:306–314

Khan MR, Li M, Mao S, Ali R, Khan S (2021b) Comparative study on heat transfer and friction drag in the flow of various hybrid nanofluids effected by aligned magnetic field and nonlinear radiation. Sci Rep 11(1):1–14

Li D, Moghaddam MR, Monjezi M, Jahed Armaghani D, Mehrdanesh A (2020) Development of a group method of data handling technique to forecast iron ore price. Appl Sci 10(7):2364

Lijima S (1991) Helical microtubules of graphitic carbon. Nature 354(6348):56–58

Mathew Nkurlu B, Shen C, Asante-Okyere S, Mulashani AK, Chungu J, Wang L (2020) Prediction of permeability using group method of data handling (GMDH) neural network from well log data. Energies 13(3):551

Mir NA, Farooq M, Rizwan M, Ahmad F, Ahmad S, Ahmad B (2020) Analysis of thermally stratified flow of Sutterby nanofluid with zero mass flux condition. J Market Res 9(2):1631–1639

Nawaz M (2020) Role of hybrid nanoparticles in thermal performance of Sutterby fluid, the ethylene glycol. Phys A 537:122447

Prashar P, Ojjela O (2022) Numerical investigation of ZnO–MWCNTs/ethylene glycol hybrid nanofluid flow with activation energy. Indian J Phys 96(7):2079–2092

Ramesh GK, Madhukesh JK (2021) Activation energy process in hybrid CNTs and induced magnetic slip flow with heat source/sink. Chin J Phys 73:375–390

Ramesh K, Rawal M, Patel A (2021) Numerical simulation of radiative MHD Sutterby nanofluid flow through porous medium in the presence of hall currents and electroosmosis. Int J Appl Comput Math 7(2):1–12

Saba F, Ahmed N, Khan U, Mohyud-Din ST (2019) A novel coupling of (CNT-Fe3O4/H2O) hybrid nanofluid for improvements in heat transfer for flow in an asymmetric channel with dilating/squeezing walls. Int J Heat Mass Transf 136:186–195

Sabir Z, Imran A, Umar M, Zeb M, Shoaib M, Raja MAZ (2021) A numerical approach for 2-D Sutterby fluid-flow bounded at a stagnation point with an inclined magnetic field and thermal radiation impacts. Thermal Sci 25(3):1975–1987

Saeed A, Alghamdi W, Mukhtar S, Shah SIA, Kumam P, Gul T, Kumam W (2021) Darcy-Forchheimer hybrid nanofluid flow over a stretching curved surface with heat and mass transfer. PLoS ONE 16(5):e0249434

Sajid T, Tanveer S, Sabir Z, Guirao JLG (2020) Impact of activation energy and temperature-dependent heat source/sink on Maxwell-Sutterby fluid. Math Probl Eng 2020:1–15

Sajid T, Jamshed W, Shahzad F, Aiyashi MA, Eid MR, Nisar KS, Shukla A (2021) Impact of Maxwell velocity slip and Smoluchowski temperature slip on CNTs with modified Fourier theory: Reiner-Philippoff model. PLoS ONE 16(10):e0258367

Sajid T, Jamshed W, Shahzad F, AkgÃ¼l EK, Nisar KS, Eid MR (2022) Impact of gold nanoparticles along with Maxwell velocity and Smoluchowski temperature slip boundary conditions on fluid flow: Sutterby model. Chin J Phys 77:1387–1404

Shanmugapriya M (2018) Analysis of heat transfer of Cu-water nanofluid flow past a moving wedge. J Inform Math Sci 10(1–2):287–296

Shanmugapriya M, Sundareswaran R, Senthil Kumar P (2021) Heat and mass transfer enhancement of MHD hybrid nanofluid flow in the presence of activation energy. Int J Chem Eng 2021:1–12
Suresh S, Venkitaraj KP, Selvakumar P, Chandrasekar M (2011) Synthesis of –Cu/water hybrid nanofluids using two step method and its thermo physical properties. Colloids Surf A Physicochem Eng Aspects 388(1–3):41–48
Sutterby JL (1966) Laminar converging flow of dilute polymer solutions in conical sections: Part I. Viscosity data, new viscosity model, tube flow solution. AIChE J 12(1):63–68
Swain K, Mebarek-Oudina F, Abo-Dahab SM (2022) Influence of MWCNT/ Fe3O4 hybrid nanoparticles on an exponentially porous shrinking sheet with chemical reaction and slip boundary conditions. J Therm Anal Calorim 147(2):1561–1570
Tassaddiq A, Khan S, Bilal M, Gul T, Mukhtar S, Shah Z, Bonyah E (2020) Heat and mass transfer together with hybrid nanofluid flow over a rotating disk. AIP Adv 10(5):055317
Tulu A, Ibrahim W (2019) Numerical analysis of heat and mass transfer flow of nanofluid over a moving wedge using spectral quasilinearization method. Int J Appl Math Theor Phys 5:111–117
Tulu A, Ibrahim W (2020) MHD slip flow of CNT-ethylene glycol nanofluid due to a stretchable rotating disk with Cattaneo-Christov heat flux model. Math Probl Eng 2020:1–13
Tulu A, Ibrahim W (2021) Effects of second-order slip flow and variable viscosity on natural convection flow of (CNT-Fe3O4/water) hybrid nanofluids due to stretching surface. Math Probl Eng 2021:1–18
Turcu R, Darabont AL, Nan A, Aldea N, Macovei D, Bica D, Biro LP (2006) New polypyrrole-multiwall carbon nanotubes hybrid materials. J Optoelectron Adv Mater 8(2):643–647
Umar M, Akhtar R, Sabir Z, Wahab HA, Zhiyu Z, Imran A, Shoaib M, Raja MAZ (2019) Numerical treatment for the three-dimensional Eyring-Powell fluid flow over a stretching sheet with velocity slip and activation energy. Adv Math Phys 2019:1–12
Wahid NS, Arifin NM, Khashi'ie NS, Pop I (2021) Hybrid nanofluid slip flow over an exponentially stretching/shrinking permeable sheet with heat generation. Mathematics 9(1):30
Waini I, Ishak A, Pop I (2020a) MHD flow and heat transfer of a hybrid nanofluid past a permeable stretching/shrinking wedge. Appl Math Mech 41(3):507–520
Waini I, Ishak A, Pop I (2020b) Squeezed hybrid nanofluid flow over a permeable sensor surface. Mathematics 8(6):898
Waini I, Ishak A, Pop I (2022) Radiative and magnetohydrodynamic micropolar hybrid nanofluid flow over a shrinking sheet with Joule heating and viscous dissipation effects. Neural Comput Appl 34(5):3783–3794
Yacob NA, Ishak A, Pop I (2011) Falkner-Skan problem for a static or moving wedge in nanofluids. Int J Therm Sci 50(2):133–139
Zainal NA, Nazar R, Naganthran K, Pop I (2021) Viscous dissipation and MHD hybrid nanofluid flow towards an exponentially stretching/shrinking surface. Neural Comput Appl 33:1–11

Publisher's Note Springer Nature remains neutral with regard to jurisdictional claims in published maps and institutional affiliations.

Springer Nature or its licensor holds exclusive rights to this article under a publishing agreement with the author(s) or other rightsholder(s); author self-archiving of the accepted manuscript version of this article is solely governed by the terms of such publishing agreement and applicable law.